HAL open science

Uncertainty analysis for seawater intrusion in fractured coastal aquifers: Effects of fracture location, aperture, density and hydrodynamic parameters

Behshad Koohbor, Marwan Fahs, Behzad Ataie-Ashtiani, Benjamin Belfort, Craig T. Simmons, Anis Younes

► To cite this version:

Behshad Koohbor, Marwan Fahs, Behzad Ataie-Ashtiani, Benjamin Belfort, Craig T. Simmons, et al.. Uncertainty analysis for seawater intrusion in fractured coastal aquifers: Effects of fracture location, aperture, density and hydrodynamic parameters. Journal of Hydrology, 2019, 571, pp.159-177. 10.1016/j.jhydrol.2019.01.052 . hal-02628584

HAL Id: hal-02628584

https://hal.inrae.fr/hal-02628584

Submitted on 21 Oct 2021

HAL is a multi-disciplinary open access archive for the deposit and dissemination of scientific research documents, whether they are published or not. The documents may come from teaching and research institutions in France or abroad, or from public or private research centers.

L'archive ouverte pluridisciplinaire **HAL**, est destinée au dépôt et à la diffusion de documents scientifiques de niveau recherche, publiés ou non, émanant des établissements d'enseignement et de recherche français ou étrangers, des laboratoires publics ou privés.

Distributed under a Creative Commons Attribution - NonCommercial 4.0 International License

Version of Record: https://www.sciencedirect.com/science/article/pii/S0022169419301234
Manuscript_1f566abd53e2c96fb93434340dc1164f

Uncertainty analysis for seawater intrusion in fractured coastal aquifers: Effects of fracture location, aperture, density and hydrodynamic parameters

Behshad Koohbor[1], Marwan Fahs[1*], Behzad Ataie-Ashtiani[2,3], Benjamin Belfort[1], Craig T. Simmons[3], Anis Younes[1,4,5]

[1]Laboratoire d'Hydrologie et Geochemie de Strasbourg, University of Strasbourg/EOST/ENGEES, CNRS, 1 rue Blessig 67084 Strasbourg, France.

[2]Department of Civil Engineering, Sharif University of Technology, PO Box 11155-9313, Tehran, Iran.

[3]National Centre for Groundwater Research & Training, College of Science & Engineering, Flinders University, GPO Box 2100, Adelaide, South Australia 5001, Australia.

[4]IRD UMR LISAH, F-92761 Montpellier, France.

[5]Laboratoire de Modélisation en Hydraulique et Environnement, Ecole Nationale d'Ingénieurs de Tunis, Tunisia

Submitted to Journal of Hydrology: Special Issue "Improving model-data interaction in Hydrogeology: Insights from different disciplines".

*Contact person: Marwan Fahs

E-mail: fahs@unistra.fr

© 2019 published by Elsevier. This manuscript is made available under the CC BY NC user license
https://creativecommons.org/licenses/by-nc/4.0/

Abstract

In this study we use polynomial chaos expansion (PCE) to perform uncertainty analysis for seawater intrusion (SWI) in fractured coastal aquifers (FCAs) which is simulated using the coupled discrete fracture network (DFN) and variable-density flow (VDF) models. The DFN-VDF model requires detailed discontinuous analysis of the fractures. In real field applications, these characteristics are usually uncertain which may have a major effect on the predictive capability of the model. Thus, we perform global sensitivity analysis (GSA) to provide a preliminary assessment on how these uncertainties can affect the model outputs. As our conceptual model, we consider fractured configurations of the Henry Problem which is widely used to understand SWI processes. A finite element DFN-VDF model is developed in the framework of COMSOL Multiphysics®. We examine the uncertainty of several SWI metrics and salinity distribution due to the incomplete knowledge of fracture characteristics. PCE is used as a surrogate model to reduce the computational burden. A new sparse PCE technique is used to allow for high polynomial orders at low computational cost. The Sobol' indices (SIs) are used as sensitivity measures to identify the key variables driving the model outputs uncertainties. The proposed GSA methodology based on PCE and SIs is useful for identifying the source of uncertainties on the model outputs with an affordable computational cost and an acceptable accuracy. It shows that fracture hydraulic conductivity is the first source of uncertainty on the salinity distribution. The imperfect knowledge of fracture location and density affects mainly the toe position and the total flux of saltwater entering the aquifer. Marginal effects based on the PCE are used to understand the effects of fracture characteristics on SWI. The findings provide a technical support for monitoring, controlling and preventing SWI in FCAs.

Keywords: Seawater intrusion, fractured coastal aquifers, uncertainty analysis, uncertain fracture characteristics, global sensitivity analysis, Sobol' indicies

1. Introduction

Coastal aquifers (CAs) are currently in a critical situation throughout the world. These aquifers are essential sources of freshwater for more than 40% of the world's population living in coastal areas *[IOC/UNESCO, IMO, FAO, UNDP, 2011; Barragán and de Andrés, 2015]*. The phenomenon of seawater intrusion (SWI), which encompasses the advancement of saline water into fresh groundwater mainly caused by excessive groundwater extraction, is the first source of contamination in CAs *[Werner et al., 2013]*. The European Environment Agency *[www.eea.europa.eu]* declared SWI as a major threat for many CAs worldwide. This phenomenon is exacerbated by the increasing demand for groundwater as a result of the increase in population and anthropogenic activity. It is also amplified due to natural causes such as climate change, Tsunami events and sea-level rise expected in the next century *[e.g., Ataie-Ashtiani et al., 2013; Ketabchi et al., 2016]*.

The impacts of local heterogeneities of CAs on the extent of SWI at the scale relevant for management scenarios is well documented in the literature *[e.g. Simmons et al., 2001; Kerrou and Renard, 2010; Lu et al., 2013; Mehdizadeh et al., 2014; Pool et al., 2015; Stoeckl et al., 2015; Shi et al., 2018]*. Fractured geology is the most challenging form of natural heterogeneity. Fractures represent the preferential pathways that may enable faster SWI or intensify freshwater discharge to the sea *[Bear et al. 1999]*. Fractured coastal aquifers (FCAs) are found globally. Several examples can be found in France *[Arfib and Charlier, 2016]*, USA *[Xu et al., 2018]*, Greece *[Dokou and Karatzas, 2012]*, Italy *[Fidelibus et al,. 2011]*, Ireland *[Perriquet et al., 2014; Comte et al., 2018]*, UK *[MacAllister et al., 2018]* and in the Mediterranean zone where more than 25% of CAs are typically karstic *[Bakalowicz et al., 2008; Chen et al., 2017]*. Despite the fact that FCAs are distributed throughout the world and they often contain significant groundwater resources due to their high porosity, SWI in these aquifers is rarely investigated and related processes are still largely unexplored and poorly understood *[Dokou and Karatzas, 2012; Sebben et al., 2015]*. In the review paper of *Werner et al. [2013]*, the authors suggested SWI in FCAs as one of the potential remaining challenging problems.

SWI can be tackled using either the sharp interface approximation or variable-density flow (VDF) model *[Werner et al., 2013; Llopis-Albert et al., 2016; Szymkiewicz et al., 2018]*. VDF model involves flow and mass transfer equations coupled by a mixture state equation expressing the density in terms of salt concentration. This model is usually used in field applications as it is more realistic than the sharp interface approximation and has the privilege of considering the transition zone between the freshwater and saltwater, known as the mixing zone. Flow in fractured porous media can be described using three alternative approaches: i) equivalent porous medium in which averaged estimations of the hydrogeological properties over a representative elementary volume are used to represent the domain *[Dietrich et al., 2005]*, ii) dual-porosity models where the domain is considered as the superposition of two continuums representing, respectively, rocks and fractures *[Fahs et al., 2014; Jerbi et al., 2017]* and iii) discrete fracture model in which the fractures and matrix are handled explicitly *[Berre et al., 2018]*. Discrete fracture model is the most accurate model because fractures are considered without any simplification. It is usually used for domains with a relatively small number of fractures *[Hirthe and Graf, 2015; Ramasomanana et al., 2018]* and has come into practical use in recent years. However, discrete fracture models require enormous computational time and memory due to the dense meshes resulting from the explicit discretization of the fractures. Discrete fracture network (DFN), in which the fractures are embedded in *(d-1)* dimensional elements in *(d)* dimensional physical domain, is an alternative approximation that reduces the overhead computations of the discrete fracture model.

DFN model has been successfully coupled with VDF model to simulate SWI in FCAs. For instance, *Grillo et al. [2010]*, based on a single fracture configuration of Henry Problem, showed that DFN-VDF model is a valid alternative to the discrete fracture model for simulating SWI. *Dokou and Karatzas [2012]* developed a hybrid model based on the combination of the DFN model (for main fractures and faults) and the equivalent porous media model (for lower-order fractures) to investigate SWI in a FCA in Greece. By confronting numerical simulations to chloride concentration observations, they showed that the DFN model is necessary to accurately simulate SWI. *Sebben et al. [2015]* used the DFN-VDF model to present a preliminary deterministic study on the effect of fractured heterogeneity on SWI, using different fractured configurations of Henry Problem. *Mozafari et al. [2018]* developed a DFN-VDF model in the finite element frame-work of COMSOL Multiphysics®. Nevertheless, the DFN-VDF model requires the basic characteristics of fractures as location, aperture, permeability, porosity, etc. These characteristics are subject to a large amount of uncertainties as they are often determined using model calibration procedure based on relatively insufficient historical data provided by several measurement techniques as surface electrical resistivity tomography *[Beaujean et al., 2014]*, borehole concentrations and head measurements, multiperiod oscillatory hydraulic tests *[Sayler et al., 2018]*, self-potential measurements *[MacAllister et al., 2018]*, among others. These uncertainties would reduce the predictive capability of the DFN-VDF model and impair the reliability of SWI management based on these predictions. Thus, it is important to understand how these uncertainties could propagate in the model and lead to uncertainty in outputs.

This work goes a step further in the understanding of SWI processes in FCAs. It aims to provide a preliminary investigation on the impacts of uncertainty associated to fractures characteristics on the extent of the steady-state saltwater wedge simulated using the DFN-VFD model. In particular, we investigate the effects of uncertainties on fracture network characteristics (location, aperture, density, permeability and dispersivity) on several SWI metrics, as the length of the saltwater toe, thickness of the mixing zone, area of the salted zone and salinity flux penetrating to the aquifer. As the underpinning conceptual model, we consider the fractured Henry Problem suggested in *Sebben et al. [2015]*. A finite element DFN-VDF numerical model is implemented using COMSOL Multiphysics® software. We include the Boussinesq approximation in the COMSOL model to reduce nonlinearity and improve computational efficiency.

In order to quantify the variability in model outputs resulting from the uncertain parameters, we use the global sensitivity analysis (GSA). GSA is more appropriate than local sensitivity analysis as it provides a robust and practical framework to explore the entire inputs space and to assess the key variables driving the model outputs uncertainty *[Saltelli, 2002; Sudret, 2008; De Rocquigny, 2012]*. GSA is a powerful approach to fully understand the complex physical processes and assess the applicability of models. It is also important for risk assessment and decision-making. In hydrogeological applications, GSA has been used to investigate saturated/unsaturated flow *[Younes et al., 2013, 2018; Dai et al., 2017; Meng and Li, 2017; Maina and Guadagnini, 2018; Miller et al., 2018]*, solute transport *[Fajraoui et al., 2011, 2012; Ciriello et al., 2013; Younes et al., 2016]*, geological CO2 sequestration *[Jia et al., 2016]*, natural convection *[Fajraoui et al., 2017]* and double-diffusive convection *[Shao et al., 2017]*. In SWI, GSA has been applied to study the effects of hydrodynamics parameters in homogeneous CAs *[Herckenrath et al., 2011; Rajabi and Ataie-Ashtiani, 2014; Rajabi et al., 2015; Riva et al., 2015; Dell'Oca et al., 2017]*. *Rajabi et al. [2015]* have shown that GSA is the best-suited method for uncertainty analysis of SWI. Recently, *Xu et al. [2018]* used GSA to investigate SWI in a karstic CA with conduit networks. To the best of our knowledge, GSA has never been applied to SWI in heterogeneous and/or FCAs. Different alternatives can be used to perform GSA [*Iooss and Lemaître, 2015*]. Among these alternatives, in this paper, we use the variance-based technique with the Sobol' indices (SIs) as sensitivity metrics *[Sobol', 2001]*. These indices are widely used because they do not assume any simplification regarding the physical model and provide the sensitivity of individual contribution from each parameter uncertainty as well as the mixed contributions *[Sarkar and Witteveen, 2016]*. SIs are usually evaluated through Monte Carlo methods which require a large number of simulations to cover the parameters space and, as a consequence, might be impractical in high CPU consuming problems (as is the case for SWI in FCAs) *[Sudret, 2008; Herckenrath et al., 2011]*. To meet the numerical challenges of Monte Carlo methods, we use the polynomial chaos expansions (PCE) which proceeds by expressing each model output as a linear combination of orthogonal multivariate polynomials, for a specified probability measure *[Crestaux et al., 2009; Konakli and Sudret, 2016; Fajraoui et al., 2017]*. In particular, we implement the sparse PCE technique developed by *Shao et al. [2017]* to allow high polynomial orders (i.e. high accuracy) with an optimized number of deterministic samples. With this technique, the number of terms in the PCE decomposition is reduced by excluding insignificant terms. The polynomial order is updated progressively until reaching a prescribed accuracy. During the procedure, Kashyap information criterion is used to measure the relevance of PCE terms *[Shao et al., 2017]*. The sparsity of the PCE allows accurate surrogate model even if the optimal number of samples necessary for a total order expansion is not achieved. Once the PCE is constructed for each model output, the SIs can be directly calculated, with no extra computational cost, by a post-processing treatment of the PCE coefficients.

The paper is organized as follows: Section 2 is for material and methods in which we present two fractured scenarios of the Henry Problem investigated in this study, the DFN-VDF model developed with COMSOL and the SWI metrics used as model outputs. Section 3 is devoted to the GSA method. In section 4, we validate the developed COMSOL model and the Boussinesq approximation by comparison against exact solutions and an in-house research code. Section 5 discusses the GSA results; it includes PCE construction, validation of PCE and uncertainties propagation. A conclusion is given in section 6.

2. Material and methods

2.1. Conceptual model: Fractured Henry Problem

The conceptual model is based on the fractured Henry Problem, suggested by *Sebben et al. [2015]*. A detailed review of the Henry Problem and its applications can be found in *Fahs et al. [2018]*. This problem deals with SWI in a confined CA of depth H and length ℓ. Sea boundary condition (constant concentration and depth-dependent pressure head) is imposed at the left side and constant freshwater flux (q_d $[L^2T^{-1}]$) with zero concentration is assumed at the right side. Two fracture configurations are investigated in our analysis. The first configuration deals with a single horizontal fracture (SHF) extending on the whole domain and located at a distance (d^F) from the aquifer top surface (Fig. 1a). This configuration is specifically considered to investigate the effect of uncertainty related to fracture location on the extent of saltwater wedge. In the second configuration, we assume a network of orthogonal fractures (NOF) (Fig. 1b), as in *Sebben et al. [2015]*. Square sugar-cube model with elementary size δ^F (distance between 2 consecutive fractures) is considered as fracture network. This configuration is considered since it allows for performing uncertainty analysis of the SWI metrics with respect to the fracture density. Furthermore, vertical fractures are important to investigate buoyancy effects.

2.2. DFN-VDF mathematical model:

Under steady-state conditions and based on Boussinesq approximation, the VDF model in the porous matrix is given by *[Guevara Morel et al., 2015]*:

$$\nabla \cdot \mathbf{q} = 0 \qquad (1)$$

$$\mathbf{q} = -K^M \left(\nabla h + \frac{\rho - \rho_0}{\rho_0} \nabla z \right) \quad (2)$$

$$\mathbf{q} \nabla c - \nabla \cdot \left(\varepsilon^M D_m \mathbf{I} + \mathbf{D} \right) \nabla c = 0 \quad (3)$$

$$\mathbf{D} = \left(\alpha_L^M - \alpha_T^M \right) \frac{\mathbf{q} \times \mathbf{q}}{|\mathbf{q}|} + \alpha_T^M |\mathbf{q}| \mathbf{I} \quad (4)$$

$$\rho = \rho_0 + \Delta\rho c \quad (5)$$

where q is the Darcy's velocity $\left[LT^{-1} \right]$; ρ_0 the freshwater density $\left[ML^{-3} \right]$; g the gravitational acceleration $\left[LT^{-2} \right]$; K^M is the freshwater hydraulic conductivity of the porous matrix $\left[LT^{-1} \right]$; h the equivalent freshwater head $[L]$; ρ $\left[ML^{-3} \right]$ the density of mixture fluid and z is the elevation $[L]$; c is the relative solute concentration $[-]$; D_m the molecular diffusion coefficient $\left[L^2T^{-1} \right]$; ε^M is the porosity $[-]$ of the porous matrix; $\mathbf{I}$ the identity matrix and $\mathbf{D}$ is the dispersion tensor; α_L^M $[L]$ and α_T^M $[L]$ are the longitudinal and transverse dispersion coefficient of the porous matrix, respectively.

With the DFN approach, the mathematical model for fractures can be obtained by assuming 1D flow and mass transport equations along the fractures direction. The resulting equations are similar to the ones in the porous matrix, but with ε^F, K^F and α_L^F as porosity, hydraulic conductivity and longitudinal dispersivity in the fractures, respectively. Transverse dispersivity in the fracture (α_T^F) is neglected, as in *Sebben et al. [2015]*. The 1D flow and mass transport equations in fracture involve the thickness of the fracture (e^F) as parameter.

2.3. DFN-VDF finite element model: COMSOL Multiphysics®:

The DFN-VDF simulations are performed using a finite element model developed with COMSOL Multiphysics® software package. COMSOL is a comprehensive simulation software environment for various applications. The use of COMSOL in applications related to hydrogeology is increasingly frequent as this software is a user-friendly tool that facilitates all the modeling steps (preprocessing, meshing, solving and post-processing) and allows an easy coupling of different physical processes *[Ren et al., 2017; Fischer et al., 2018]*. Our COMSOL model is created by coupling the "Subsurface Flow" and "Transport of Diluted Species" modules and by assuming concentration-dependent fluid density. The Subsurface Flow module is an extension of COMSOL modeling environment to applications related to fluid flow in saturated and variably saturated porous media. In this module, we use the "Darcy's Flow" interface. The fractures are included via the DFN model by adding the "Fracture Flow" feature to the "Darcy's law" interface. The "Transport of Diluted Species" module is used to solve the advection-dispersion equation. The Boussinesq approximation is implemented by considering constant density in the fluid properties and setting a buoyancy volume force depending on the salt concentration. The numerical scheme suggested by default in COMSOL is used to solve the system of equations. The flow and transport models are solved sequentially via the segregated solver. Accurate solutions of the flow model can be obtained using finite volume or finite difference methods *[Deng and Wang, 2017]*. However, in COMSOL, quadratic basis finite element functions are used for the discretization of the pressure in the flow model while the concentration in the transport model is discretized using the linear basis functions. The consistent stabilization technique is used to avoid unphysical oscillations related to the discretization of the advection term. This technique is often called upwinding. It adds diffusion in the streamline direction. Triangular meshes suggested by the COMSOL meshing tool are used in the simulations. With the DFN model, the COMSOL meshing tool generates 2D triangular cells to represent the matrix and 1D cells to represent the fractures. The fracture cells are positioned along the sides of the matrix triangular cells. With the finite-element modeling framework, the common degrees of freedom at the triangle nodes in the matrix and at the 1D segments in the fractures are used to model the volumetric and mass fluxes between the matrix and the fractures. First runs have shown that, with the steady-state mode, COMSOL is bound to run into convergence difficulties. To avoid this problem, we used the transient mode. This problem is related to the initial guesses, required for the nonlinear solver, that are often hard to obtain. Hence, the steady-state solutions are obtained by letting the system evolve under transient conditions until steady-state.

2.4. Metrics Design:

The main purpose of this study is to perform GSA in regards to certain metrics characterizing the steady state salt-wedge and saltwater flux associated with SWI. The model inputs will be discussed later in the results section since they are dependent on the fracture configuration. As model outputs, we consider the following SWI metrics:

- The spatial distribution of the salt concentration: It is obtained in a pattern of a 100×50 regular 2D square grid (5,000 nodes).
- Length of the saltwater toe (L_{toe}): The distance from sea boundary to the 0.5 isochlor on the bottom surface of the aquifer (Fig. 2).
- Thickness of the saltwater wedge (L_S): The distance between the 0.1 and 0.9 isochlors on the aquifer bottom surface (Fig. 2).
- Average horizontal width of the mixing zone ($\overline{W}_{mz}$): The average horizontal distance between the 0.1 and 0.9 isochlors from the bottom to the top of the aquifer (Fig. 2).
- The height of the inflection point (Z_I): The freshwater-seawater inflection point located on the seaward boundary (Fig. 2). Below this point, the seawater flows toward the land, and above it the freshwater is discharged to the sea.

- The dimensionless mass of salt persisting in the aquifer $\left(M_S = \frac{1}{\ell . H} \int_0^{\ell} \int_0^{H} c.dxdz \right)$: The double integral is calculated with the grid used for the spatial distribution of salt concentration. Only nodes with concentration above 0.01 are considered.
- Total dimensionless flux of saltwater entering the aquifer (Q_S^{total}): defined as the flux of saltwater entering the domain by advection, diffusion and dispersion normalized by the freshwater flux imposed at the inland boundary (q_d).

3. Global sensitivity analysis

GSA is a useful and a widespread tool that aims to quantify and evaluate the output uncertainties resulting from the uncertainties in the model inputs, which could be considered singly (for one parameter) or coupled together (several parameters). In this study, the variability of the model responses is quantified throughout a variance based technique using SIs as sensitivity metrics. On the one hand, variance-based sensitivity measures are of interest as they typically specify the relationship between model outputs and input parameters. And on the other hand, the major advantage of using SIs is that they do not require any assumptions of monotonicity or linearity in the physical model. The main stages of this technique are developed here. More details can be found in *Sudret [2008]*, *Fajraoui et al.* [2017] and *Le Gratiet et al. [2017]*

Let us consider a mathematical model, $Y = \mathrm{M}(\mathbf{X})$, delivering the outputs of a physical system that presumably depends on M-uncertain input parameters $\mathbf{X} = \{X_1, X_2, ..., X_M\}$. For further developments, $f_{Xi}(x_i)$ and $f_x = \prod_{i=1}^{M} f_{X\,i}(x_i)$ refer to their marginal probability density function (PDF) and the corresponding joint PDF of a given set.

3.1 Sobol' indices

The Sobol' decomposition of $\mathrm{M}(\mathbf{X})$ reads *[Sudret, 2008; Fajraoui et al., 2017]*:

$$\mathrm{M}(\mathbf{X}) = \mathrm{M}_0 + \sum_{i=1}^{M} \mathrm{M}_i(X_i) + \sum_{1 \le i < j \le M} \mathrm{M}_{ij}(X_i, X_j) + \ldots + \mathrm{M}_{1,2,\ldots,M}(X_1, \ldots, X_M), \tag{6}$$

where M_0 is the expected value of $\mathrm{M}(\mathbf{X})$ and the integral of each summand $\mathrm{M}_{i_1, i_2, \ldots, i_s}(X_{i_1}, X_{i_2}, \ldots, X_{i_s})$ over any of its independent variables is zero, that is:

$$\int_{\Gamma_{X_{i_k}}} \mathrm{M}_{i_1, i_2, \ldots, i_s}(X_{i_1}, X_{i_2}, \ldots, X_{i_s}) f_{X i_k}(x_{i_k}) = 0 \text{ for } 1 \le k \le s, \tag{7}$$

where $f_{X i_k}(x_{i_k})$ and $\Gamma_{X_{i_k}}$ represent the marginal PDF and support of X_{i_k}, respectively.

The orthogonality M_i leads a unique Sobol' decomposition:

$$\mathrm{E}[\mathrm{M}_u(X_u)\mathrm{M}_v(X_v)] = 0, \tag{8}$$

Where, $\mathrm{E}[.]$ is the mathematical expectation operator, $u = \{i_1, i_2, \ldots, i_M\} \subseteq \{1, 2, \ldots, M\}$ represents the index sets and X_u are the subvectors involving the components for which the indices belong to *u*. As a result of uniqueness and orthogonality of Y, its total variance *D* is decomposed as below:

$$D = \mathrm{Var}[\mathcal{M}(X)] = \sum_{u \neq 0} D_u = \sum_{u \neq 0} Var[\mathcal{M}_u(X_u)], \tag{9}$$

where D_u is the partial variance expressed as below:

$$D_u = Var[\mathcal{M}_u(X_u)] = E[\mathcal{M}_u^2(X_u)] \tag{10}$$

Consequently, the SIs are naturally defined as:

$$S_u = \frac{D_u}{D} \tag{11}$$

The influence on *Y*, of each parameter (considered singly), is given by the first order Sobol' indices (S_i) defined by:

$$S_i = \frac{D_i}{D} \tag{12}$$

The total SI that includes the effect of an input parameter with the contribution from other parameters, is defined as follows *[Homma and Saltelli, 1996]*:

$$S_i^T = \sum_{\vartheta_i} \frac{D_u}{D}, \qquad \vartheta_i = \{u \supset i\} \tag{13}$$

The SIs can be calculated by performing Monte-Carlo simulations. This can be done using the estimates of the mean value, total and partial variance of a large number of samples, as explained in Sudret [2008]. The drawback of Monte-Carlo simulations lies in the computational cost especially when time-consuming models are investigated. To circumvent this problem, *Sudret [2008]* introduced the PCE for the computation of SIs.

3.2 Polynomials chaos expansion (PCE)

Each model output is expanded into a set of orthonormal multivariate polynomials of maximum degree M:

$$Y = M(X) \approx \sum_{\alpha \in A} y_\alpha \Phi_\alpha(X), \tag{14}$$

where *A* is a multi-index $\alpha = \{\alpha_1, \alpha_2, ..., \alpha_M\}$ and $\{y_\alpha, \alpha \in A\}$ are the polynomial coefficients. $\Phi_\alpha(X)$ are the base functions of vector space of polynomial functions. These functions should be orthogonal in the vector space with the joint PDF f_X of X as a dot product.

The polynomial coefficients $\{y_\alpha\}$ are evaluated using the regression method (least-square technique) that proceeds by minimizing an objective function representing the difference between the meta-model and physical model (see Fajraoui et al. [2017]). Based on the PCE, the mean value (μ) and total variance (D) of any model output can be calculated as follows:

$$\mu = y_0 \tag{15}$$

$$D = \sum_{\alpha \in A \backslash 0} y^2{}_{\alpha} \tag{16}$$

Then the SIs of any order can be computed using the coefficients, D and μ in a straightforward manner as followed:

$$S_i = \sum_{\alpha \in A_i \backslash 0} y^2{}_{\alpha} / D, \qquad A_i = \{\alpha \in A : \alpha_i > 0, \alpha_{j \neq i} = 0\}, \tag{17}$$

and

$$S_i^T = \sum_{\alpha \in A_i^T \backslash 0} y^2{}_{\alpha} / D, \qquad A_i^T = \{\alpha \in A : \alpha_i > 0\} \tag{18}$$

As suggested by *Deman et al. [2016]*, we also evaluate the marginal effect (ME) to understand the relation between the important variables and the model outputs. ME is given by:

$$E[\mathcal{M}(X) \mid X_i = x_i] = \mathcal{M}_0 + \sum_{\alpha \in A_i} y_{\alpha} \Phi_{\alpha}(x_i) \tag{19}$$

3.3 Sparse polynomial chaos expansion

To minimize the number of physical model evaluations and therefore reduce the computational cost, the estimation of the Sobol' indices could be done with a sparse PCE instead of a full PCE approach. In other words, instead of using the expression Eq. (14), we can only use some relevant coefficients of the PCE. The key idea consists in discarding the irrelevant terms in the estimated truncated PCE and for this purpose, several approaches have been developed. *Blatman and Sudret [2010]* utilized an iterative forward–backward approach based on nonintrusive regression or a truncation strategy based on hyperbolic index sets coupled with an adaptive algorithm involving a least angle regression (LAR). *Meng and Li [2017]* modified the LAR algorithm with a least absolute shrinkage and selection operator (LASSO-LAR). An adaptive procedure using projections on a minimized number of bivariate basis functions has been provided by *Hu and Youn [2011]*, whereas *Fajraoui et al. [2012]* worked with a fixed experimental design and retained only significant coefficients that could contribute to the model variance. The approach developed in *Shao et al. [2017]*, which has been implemented in this work, consists in progressively increasing the degree of an initial PCE until a satisfactory representation of the model responses is obtained. The computation of the Kashyap information criterion (KIC) based on a Bayesian model averaging is used to determine the best sparse PCE for a input/output sample. Evaluating KIC is an efficient (from a computational point of view) and feasible alternative to directly computing the Bayesian model evidence, being known that this later evaluates the likelihood of the observed data integrated over each model's parameter space. Hence, it is a key term to obtain the posterior probability in the Bayesian framework. For more details on the Bayesian sparse PCE, for constructing the algorithm and computing the KIC, readers can refer to *Shao et al. [2017]*.

4. Validations: COMSOL model and Boussinesq approximation

Although COMSOL has great potential for modelling density-driven flow problems, it has rarely been used for SWI. Thus, the main purpose of this section is to validate our developed COMSOL model. In addition, as explained previously, Boussinesq approximation was implemented in our COMSOL model to improve its computational efficiency. This is a popular approximation for the VDF model as it allows for reducing the computational costs and renders convergence more likely to be achieved. It assumes that variations in density only give rise to buoyancy forces and have no impact on the flow field. Boussinesq approximation ignores density-concentration dependence except in the buoyancy term. This approximation is common for SWI in non-fractured CAs *[Guevara Morel et al., 2015]*. Its validity for SWI in FCAs is not discussed in the literature. Thus, another goal of this section is to investigate the validity of this approximation for such a case.

For this purpose, we first use the new semi-analytical solutions of the Henry Problem (homogeneous aquifer) developed by *Fahs et al. [2016]*. We compare these solutions against two COMSOL models: i) SWI-COMSOL model based on the standard COMSOL approach and ii) SWI-COMSOL-Bq based on the Boussinesq approximation. We investigate two test cases presented in *Fahs et al. [2016]* which deal with constant and velocity-dependent dispersion tensor, respectively. The corresponding physical parameters are summarized in Table 1. It is noteworthy that, for the validation cases, similar to the semi-analytical solution, the sea boundary is assumed at the right side of the domain. The main isochlors (0.1, 0.5 and 0.9) obtained with COMSOL models as well as the semi-analytical ones are plotted in Fig. 3. The corresponding SWI metrics are given in Table 2. The COMSOL simulations have been performed using a mesh consisting of about 18,000 elements. As is obvious from Fig. 3, excellent agreement is obtained between the COMSOL and the semi-analytical results. This highlights the accuracy of the developed COMSOL models and the related post-treatment procedure applied to obtain the SWI metrics. It also confirms the validity of the Boussinesq approximation for SWI in homogenous CAs.

For FCAs, analytical or semi-analytical solutions do not exist. We compare the developed COMSOL models (SWI-COMSOL and SWI-COMSOL-Bq) against an in-house research code (TRACES) based on advanced space and time discretization techniques *[Younes et al., 2009]*. This code has been validated by comparison against several configurations of semi-analytical solutions in *Fahs et al. [2018]*. It has proven to be a robust tool for the simulation of SWI in both homogeneous and heterogeneous domains. DFN approach, which is based on average properties over the fracture width, is not available in TRACES. Thus, the fractures are modeled by considering heterogeneity of material without reduction of the dimensionality; i.e. fracture is a specific layer of the 2D domain with different assigned properties. We considered two validation cases which are based on a single horizontal and vertical fractures, respectively. The horizontal fracture is located at the aquifer middle-depth $(d^F = 0.5m)$ while the vertical fracture is located near the seaside at $x=1.8$m. The physical parameters are given in Table 1. The mesh used in the COMSOL simulations involves about 50,000 elements. In the in-house code we use a mesh with about 70,000 elements. The obtained main isochlors are given in Fig. 4 and the corresponding SWI metrics are summarized in Table 2. Fig. 4a shows that, in the case of single horizontal fracture, the high conductivity in the fracture increases the freshwater discharge to the sea and pushes the saltwater wedge toward the sea, especially around the fracture. In the case of vertical fracture (Fig. 4b), the high permeability in the fracture enhances the upward flow and push up the saltwater around the fracture Fig. 4 and Table 2 show excellent agreement between COMSOL and TRACES. They confirm the validity of the Boussinesq approximation in the presence of fractures and highlight the accuracy of the developed COMSOL model. It should be noted also that the comparison between the COMSOL model (in which the fracture is considered as a line) and TRACES (in which the fracture is a 2D layer) confirms the results of *Grillo et al. [2010]* about the validity of the technique based on *(n-1)* dimensional fractures (i.e. average properties over the fracture) for the simulation of SWI in FCAs.

5. Global sensitivity Analysis: results and discussion

The methodology used to perform GSA is described in the flowchart presented in Fig. 5. In this section we present the assumptions and numerical details related to the PCE construction. We also validate the PCE meta-model by comparison against physical COMSOL model and we present the results of the GSA based on the SI's, for both salinity distribution and SWI metrics.

5.1 The single horizontal fracture configuration (SHF)

Several studies showed that, under steady-state condition, the isotropic Henry Problem is governed by six dimensionless quantities which are the gravity number, longitudinal and transverse Peclet numbers, ratio of the fresh water density to the difference between freshwater and saltwater densities, Froude number and the concentration of salt in seawater *[Riva et al., 2015; Fahs et al., 2018]*. Uncertainty analysis related to these parameters is performed in *Riva et al. [2015]*. The main goal of our work is to investigate the effect of uncertainties related to the presence of fractures. Thus, for the SHF configuration, we assume that the hydraulic conductivity (K^F), aperture (e^F), depth (d^F) and longitudinal dispersivity (α_L^M) of the fracture are uncertain. For the matrix domain, we only include the longitudinal dispersivity (α_J^M) in our analysis as this parameter is important for the exchange between fracture and matrix domain. The dispersivity ratio (transverse to longitudinal) is set to be 0.1. Other parameters are kept constant. Table 3 summarizes the values of the deterministic parameters as well as the range of variability of the uncertain parameters. The values used in this table are similar to *Sebben et al. [2015]*.

We should mention that network connectivity (i.e. how fractures are interconnected) has a clear and large impact on the extent of SWI. However, in the cases investigated in this work, all the fractures are fully connected (abutting and crossing fractures). Thus the effect of network connectivity is not considered. Disconnected cases are not considered because it is not obvious to find well defined parameters (required for GSA) to describe the connectivity. Also, disconnected fractures can lead to discontinuous model outputs for which the PCE surrogate model could not approximate the true system with an acceptable degree of accuracy.

- *PCE construction: Numerical details, orders and accuracy*

The uncertain parameters are assumed to be uniformly distributed over their ranges of variability. The PCEs are evaluated using an experimental design consisting of 100 samples. To obtain a deterministic experimental design that covers the parameter space, we use the Quasi-Monte-Carlo sampling technique. A preliminary mesh sensitivity analysis is performed to ensure mesh-independent solutions for all the simulated samples. These simulations were important in order to verify that the GSA results are not affected by numerical artifacts related to the finite element discretization. The mesh sensitivity analysis is performed using the most challenging numerical case that deals with the highest value of K^F and lowest values of α_L^M, α_L^F and e^F. In such a case the advection and buoyancy processes are very important and the corresponding numerical solution could be highly sensitive to the mesh size as it might suffer from unphysical oscillations or numerical diffusion. A mesh-independent solution is achieved for this case using a grid consisting of about 50,000 elements. This mesh is used for the 100 simulations required for computing the PCE expansions.

For each SWI metric (or model output), the corresponding PCE surrogate model is calculated using the technique described in section 3. For the salt concentration distribution (multivariate output), component-wise PCE is constructed on each node of the regular 2D square grid defined for the control points (involving 5,000 control points). The MATLAB code developed by *Shao et al. [2017]* is used to compute the sparse PCE. To give more confidence to the sparse PCE, we also compute total order PCE using the UQLAB software *[Marelli and Sudret, 2014]*. As five input variables are considered and 100 samples are available, only third-order polynomial could be reached via the total order PCE expansion. The corresponding optimal number of samples is 56. With the sparse technique, implemented in this work, higher orders can be reached even if the optimal number of samples required for full PCE is not achieved. Sixth order PCE is reached for the salt concentration distribution and all SWI metrics except the width of the mixing zone for which the polynomial order is limited to five. The accuracy of the resulting sparse PCE surrogate model is checked by comparison against the physical COMSOL model. In Fig. 6, we compare the values obtained with the sparse PCE with those of DFN-VDF physical model implemented with COMSOL for parameter inputs corresponding to the experimental design (i.e. used for the PCE construction) and also for new samples. Some examples of the results, precisely the length of saltwater toe $\left(L_{toe}\right)$ and the mass of salt persisting in the aquifer (*Ms*), are plotted in Fig. 6. We can observe an excellent match which confirms that the PCE surrogate model reproduces the physical model outputs well.

- *Uncertainty propagation and Marginal Effects (ME)*

Based on the PCE, we calculate the first and total SIs which are used for uncertainty propagation. We also calculate the ME (univariate effect) to obtain a global idea about the impact of the input parameters on the model output. The ME of a certain parameter represents the variability of the model output to this parameter when other parameters are kept constant, at their average values.

The GSA results for the spatial distribution of the salt concentration are illustrated in Fig. 7. Fig. 7a shows the distribution of the mean concentration based on the PCE expansion. At each node of the mesh used for the control points, the mean value of the salt concentration is calculated as the arithmetic average of the concentrations corresponding to the 100 samples used in the experimental design which are evaluated via the PCE surrogate model. This figure shows that the mean concentration distribution reflects the systematic behavior of SWI. The isochlors are more penetrated at the bottom aquifer due to the saltwater density. This confirms that the PCE surrogate model mimics the full model’s response. We also calculate the concentration variance to evaluate how far the concentrations are spread out form their average values (Fig. 7b). As expected, the variance is significant in the saltwater wedge. The largest values are located near the aquifer bottom surface where the SWI is usually induced by mixing processes that can be highly sensitive to the model inputs (fracture characteristics and matrix dispersivity). The variance is negligible near the sea-side as the boundary conditions are almost deterministic and the sole acting random parameter is the longitudinal dispersivity that can affect the dispersive entering flux. The sensitivity of the concertation distribution to the uncertain parameters is assessed with the maps of the total SI (Figs 7 c-g). The total SI of α_L^M (Fig. 7c) shows that the uncertainty related to this parameter affects the concentration distribution at the top aquifer, outside the saltwater wedge. In this zone, the salt transport processes are dominated by the longitudinal dispersion flux as the velocity is toward the sea and it is almost horizontal and parallel to the salt concentration gradient. The zones of largest total SI for K^F and e^F are located within the saltwater wedge toward the low isochlors (Fig. 7d and 7e). In this region, the mass transfer is mainly related to the advection process which is related to the velocity field. This later is highly depending on the fracture permeability and aperture. The zone of influence of d^F is also located within the saltwater wedge, but toward the aquifer bottom surface and at the vicinity of the high isochlors (Fig. 7f). The influence of α_L^F is limited to the vicinity of the sea boundary where α_L^F can impact the saltwater flux to the aquifer (Fig. 7g). In the fracture, advection is dominating and dispersion is negligible. It is worthwhile noting that the total SIs count in the overall contribution of a parameter including nonlinearities and interactions. Thus, SIs allow for ranking the parameters according to their importance. It appears on Figs. 7 that d^F, K^F and e^F are the most influential parameters because their total SI are more pronounced in the region where the salt concentration variance is maximum. From the scales of Figs. 7 (d-f), it is clear that K^F and e^F are more influential than d^F. Figs. 7c shows that the salinity distribution is weakly sensitive to the longitudinal dispersivity of the matrix as in its zone of influence the variance is negligible.

Inspection of the sensitivity of SWI metrics to uncertain parameters is given in Fig. 8. This figure represents the bar-plots of the total and first-order SIs of the SWI metrics. As mentioned previously for a further understanding of the uncertainty on SWI metrics related to the imperfect knowledge of input parameters, we also investigate the MEs of the most relevant parameters. These MEs are plotted in Fig. 9. The large variability of the SWI metrics (see vertical scales in Figs. 9a-j) confirms that the MEs are in agreement with the SIs.

Fig. 8a shows that the uncertainty on L_{toe} is mainly due to the effects of d^F and K^F. With a total SI of 0.54, d^F is considered as the most influential parameter. The ME of d^F and K^F on L_{toe} are given in Fig. 9a and 9b, respectively. Fig. 9a shows that L_{toe} decreases with d^F which is coherent with the results of *Sebben et al. [2015]*. Fig. 9b shows that L_{toe} increases with K^F. The physical interpretation of this variation is that the increase of K^F heightens the potential of the fracture to constitute a preferential freshwater flow path. This slow down the freshwater flow in the matrix which in turn facilitates SWI and leads to the increase of the penetration length of the saltwater wedge. Fig. 8b indicates that the variability of L_S is mainly impacted by α_L^M . This makes sense as L_S measures the salinity dispersion along the aquifer bottom surface which is mainly controlled by α_L^M . L_S is even expected to increase with α_L^M , which is confirmed from the ME in Fig. 9c. We can also notice in Fig. 8b the slight sensitivity of L_S to d^F. The corresponding ME (Fig. 9d) shows that this sensitivity is relatively important for deep fractures ($d^F > 0.6$).

The SIs for $\overline{W}_{mz}$ are given in Fig. 8c. The width of the mixing zone is mainly controlled by the dispersive flux. This is why, α_L^M is the main parameter affecting $\overline{W}_{mz}$. As expected, increasing variation of $\overline{W}_{mz}$ against α_L^M can be observed in Fig. 9e. For Z_I (Fig. 8d), with a total SI of 0.58, d^F is the most important parameter. Fig. 9f shows that Z_I decreases with d^F, which is in agreement with the results of *Sebben et al. [2015]*. Variability of Z_I could be also affected by the uncertainty of K^F. The corresponding ME in Fig. 9g shows that Z_I increases with K^F. Fig. 8e depicts the SIs for the mass of salt persisting in the aquifer $\left(M_S\right)$. It indicates that M_S is primarily sensitive to d^F (SI=0.62). It is also sensitive to K^F. ME (Fig. 9h) shows that M_S decreases with d^F, which is also consistent with the results *Sebben et al. [2015]*. M_S increases with K^F (Fig. 9i). This behavior is related to fact that the increase of K^F enhances the inland extent of the saltwater wedge, as explained in the previous section. Finally, the SIs for Q_S^{total} shows that this output is mainly affected by d^F (Fig. 8f). As show in Fig. 9j (Q_S^{total}) increases with d^F. In general, the SIs show that the uncertainty associated with α_L^F has no effect on the SWI metrics, which is logical, as salt transport in the fracture is dominated by the advection processes.

5.2 The network of orthogonal fractures configuration (NOF)

In this configuration, our goal is to investigate the effect of uncertainty related to the fractures density on the model outputs. Thus, we keep the same uncertain parameters as for the SHF configuration but we replace (d^F) by (δ^F). The latter is considered here as the parameter representing the fracture density. The values of the deterministic parameters and the range of variability of the uncertain inputs are given in Table 3. The lowest value of δ^F corresponds to a network with 13 horizontal and 26 vertical fractures. These values are used to obtain the results in affordable CPU time, as denser fractured configurations would require a large number of simulations to construct the PCE and the COMSOL model in this case becomes very CPU time consuming. We should mention that, for this configuration, we reduce the hydraulic conductivity of the fractures. If the same values would have been used as in SHF configuration, freshwater flow would have been so intensive that no SWI would occur.

- *PCE construction: Numerical details, orders and accuracy*

The NOF configuration is more sensitive to the fractures characteristics than SHF configuration. The number of samples is progressively increased until obtaining accurate PCEs. The corresponding experimental design involves 200 samples. The mesh sensitivity analysis for the most challenging cases (the smallest value of δ^F) reveals that mesh-independent solution can be obtained using a grid of 70,000 elements. As for the SHF configuration, sparse and total PCE are calculated. With 200 samples, order 4 total PCE can be obtained. The optimal number of samples is 126. With the sparse technique, sixth order polynomial is reached for L_{toe}, M_S, Z_I and Q_S^{total}. For L_S and $\overline{W}_{mz}$ orders 4 and 8 are achieved, respectively. Fig.10 shows some comparisons between the sparse PCE surrogate and COMSOL models and highlights the accuracy of the PCE expansions. A good matching is observed both for the input parameters of the experimental design and for new samples. It is relevant to emphasize that this level of accuracy is acceptable to obtain good GSA results with the SIs evaluated using the surrogate model.

- *Uncertainty propagation and marginal effects*

The distribution of the mean concentration based on the PCE expansion is given in Fig. 11a. The mean PCE isochlors emulate the ones obtained using the physical model (Fig. 12). They present some discontinuous points where saltwater is pushed toward the sea due to high permeability in the fractures. The spatial map of the concentration variance is plotted in Fig. 11b. Compared to the SHF configuration, the zone of significant variance is contracted and concentrated toward the bottom surface of the aquifer near the low mean isochlors. The map of the total SIs of α_L^M (Fig. 11.c) is quite similar to the one in the SHF configuration but it echoes the presence and influence of fracture network. Fig.11c shows that the zone of influence of α_L^M falls where the concentration variance is negligible. Thus, α_L^M is not an important parameter for salinity distribution. Sensitivity to K^F and e^F are both important (Fig. 11d and e). The zone of influence of K^F is discontinuous and mainly located toward the sea boundary in at the bottom of the aquifer. Important values can be observed landward (see Fig. 11. d) but these values do not express high sensitivity as the concentration variance is negligible in this zone. The sensitivity to the fractures density (δ^F) is given in Fig. 11f. This figure shows that uncertainty associated δ^F can mainly affect the salinity distribution within the mixing zone toward the bottom surface. It confirms that δ^F is an influential parameter. Finally, and in contrast to the SHF configuration, α_L^F appears to be an important parameter in the NOF configuration (Fig. 11g). It affects mainly salinity distribution around the low isochlors.

The bar-plots in Fig. 13 depict the total and first-order SIs for the SWI metrics to the uncertain parameters and Fig. 14 gives the MEs of these parameters. In general Fig. 14 confirms the results of the SIs as large variations of SWI metrics can be observed with respect to the uncertain parameters. Fig. 13a demonstrates that L_{toe} is mainly controlled by K^F and δ^F. The corresponding total SIs are $S_{K^F}^T = 0.52$ and $S_{\delta^F}^T = 0.32$, respectively. Fig. 14a shows an increasing variation of L_{toe} against K^F. As for the SHF configuration, this is related to the fact that the increase of K^F concentrates the freshwater flow in the fractures and entails a weaker freshwater flow in the matrix. As consequence, the saltwater wedge expands landward and L_{toe} increases. This behavior can be understood also using the equivalent porous media model which is based on a bulk hydraulic conductivity. As given in *Sebben et al. [2015]*, the bulk equivalent conductivity (K^{eq}) for a network of orthogonal fractures is given by:

$$K^{eq} = \left[\left(K^M + \frac{K^F e^F}{\delta^F} \right)^{-1} + \frac{e^F}{K^F \delta^F} \right]^{-1} \quad (20)$$

Eq. (20) shows that K^{eq} increases with the increase of K^F. The equivalent gravity number, which compares the buoyancy forces to the inland freshwater flux, is given by *[Fahs et al. 2018]*:

$$Ng^{eq} = \frac{K^{eq}.H.(\rho_1 - \rho_0)}{\rho_0 q_d} \quad (21)$$

The increase of K^{eq} leads to the increase of Ng^{eq}. This latter can be interpreted, at constant densities and hydraulic conductivity, as a decrease in the inland freshwater that opposes SWI. This enhances the extend of SWI and leads to the increase of L_{toe}.

Fig. 14b shows that L_{toe} decreases with δ^F. In fact, the increase of δ^F corresponds to the reduction of the fracture density. This enhances the freshwater flow in the porous matrix and pushes the saltwater wedge toward the sea. The equivalent bulk hydraulic conductivity model can be also useful in explaining this variation, by reasoning in the same way as for the variation of L_{toe} against K^F. As it is clear from Eq. (20), the increase of δ^F (for the average value of K^M, K^F and e^F) corresponds to a decrease in K^{eq} and the related equivalent gravity number. This can be interpreted as an increase of the freshwater flux that lowers the extent of SWI and decreases L_{toe}.

The bar-plots in Figs. 13b and 13c indicate that, as for the SHF configuration, α_L^M is the most important parameter affecting L_S and $\overline{W}_{mz}$. The corresponding SIs are calculated to be 0.68 and 0.34, respectively. Figs. 14c and 14d display increasing variation of L_S and $\overline{W}_{mz}$ against α_L^M. This makes sense as L_S and $\overline{W}_{mz}$ are mainly related to the mixing processes which are controlled by α_L^M. Fig. 13d shows that, with $S_{K^F}^T = 0.50$ and $S_{\delta^F}^T = 0.27$, K^F and δ^F are the most important parameters affecting Z_I. MEs in Figs. 14e and 14f indicate that Z_I increases with K^F and decreases with δ^F. The reason behind these variations is the enhancement (resp. reduction) in the saltwater wedge extent associated with the variation of K^F (resp. δ^F), explained previously. These results related to the variation of Z_I against δ^F are found to be in agreement with those in *Sebben et al. [2015]*.

The dimensionless mass of salt persisting in the aquifer (M_S) appears to be sensitive to all uncertain parameters, except α_L^F (Fig. 13e). The total SIs with respect α_L^M, K^F, e^F, δ^F are calculated to be 0.34, 0.41, 0.22 and 0.27, respectively. The MEs show that M_S decreases with δ^F and increases with K^F and α_L^M (Figs. 14g-i). The variation against δ^F and K^F is related to the behavior of the saltwater wedge when these parameters change (see above). The increase of α_L^M pushes the saltwater wedge landward *[Fahs et al., 2018]* and increases the area of the salted zone as well as the mass of salt persisting in the aquifer. The total flux of saltwater entering the aquifer (Q_S^{total}) is mainly affected by α_L^M, K^F (Fig. 13f). The total SIs of these parameters are calculated to be 0.43 and 0.42, respectively. The MEs (Figs. 14j and 14k) show that Q_S^{total} increases with α_L^M and decreases with K^F. Indeed, Q_S^{total} is advective and dispersive saltwater flux at the sea boundary. The dispersive flux is proportional to α_L^M. This explains why Q_S^{total} increases with α_L^M. The increase of K^F corresponds to the decrease of the gravity number (see above). A lower gravity number indicates less significant effect of the buoyancy forces for which the saltwater velocity decreases and reduces the advective saltwater flux. Finally, it is worth noting that, for the NOF configuration, the SIs for α_L^F are more important than for the SHF configuration. α_L^F appears to be an important parameter, especially for L_{toe} and L_s. In general, physical consistency of the results for both SHF and

NOF configuration provides insight on the validity of our analysis based on the PCE as a meta-model.

5. Conclusion

In this work, the DFN model is coupled with the VDF model to simulate SWI in FCAs. The DFN-VDF model requires the discontinuous description of the fracture characteristics which are usually uncertain. Thus, it is essential, for several practical and theoretical purposes, to understand/quantify how the uncertainties associated with the imperfect knowledge of the fracture characteristics can propagate through the model and introduce uncertainties into the model outputs. Despite the high performance of computer codes for SWI models, run-time of these codes is still high because of the high nonlinearity, dense grids required for fractures and large space and time scales associated with studied domains. Thus the traditional techniques for uncertainty analysis (i.e. Monte-Carlo simulations) cannot be easily applied in this context, as they require a large number of simulations to achieve reliable results. To meet the computational challenges of traditional techniques, we develop in this work a GSA based on the non-intrusive PCE. In particular, we apply an efficient sparse technique to construct the PCE with a reduced number of model evaluations, based on Kashyap information criterion. In the literature, GSA has been recently applied to SWI but previous studies are limited to homogeneous domain. Two configurations of the fractured Henry Problem, dealing with a single horizontal fracture (SHF) and a network of orthogonal fractures (NOF), are considered as conceptual models. The simulations required to construct the PCE are performed using a finite element model developed in the framework of COMSOL software. Boussinesq approximation is implemented to improve the computational efficiency of the COMSOL model. From technical point of view, this work shows several novelties that are important for the simulation of SWI. It shows the ability of COMSOL to accurately simulate SWI in simple and fractured aquifers. It also proves that the dimension reduction of fractures in the frame of the DFN model is a valid approach to simulate SWI in FCAs and confirms the validity of the Boussinesq approximation in such a case. Regarding uncertainty analysis, this study presents an efficient (low cost) methodology to understand uncertainty propagation into SWI models. This methodology is generic and can be efficiently applied to real field investigations. In hydrogeological applications, GSA is often applied to investigate uncertainty propagation associated with hydrogeological parameters. This work shows that GSA is generic and can be a valuable tool for different kinds of uncertainties. The GSA results showed that, for the SHF configuration, the uncertainty associated with the fracture hydraulic conductivity and depth is the first sources of uncertainty on the salinity distribution. The spatial distributions of the SIs are given as maps. This represents an important feature of this study as these maps are not only important for uncertainty analysis but also provide relevant locations for measurement required for aquifer characterization. Fracture hydraulic conductivity and depth are also important parameters for the toe position (L_{toe}), thickness of the freshwater discharge zone $\left(Z_I\right)$, the mass of salt persisting in the aquifer $\left(M_S\right)$ and the flux of saltwater entering the aquifer $\left(Q_S^{total}\right)$. The thickness of the saltwater wedge and the width of the mixing zone are mainly controlled by the dispersion coefficient in the matrix. The uncertainty related to the fracture aperture has a slight impact on the SWI metrics. Its major effect is observed on L_{toe}. Uncertainty associated with the fracture dispersion coefficient does not affect in any way the SWI metrics. For the NOF configuration, the imperfect knowledge of fracture hydraulic conductivity and density are the first source of uncertainty of the salinity distribution. However, it is observed that all the uncertain parameters become important for the salinity distribution, in this case. In contrast to the SHF configuration, in which the dispersion in the fracture is not important, in the NOF configuration the salinity distribution at the aquifer top surface is influenced by this fracture dispersivity. L_{toe} and Z_I are mainly controlled by the fractures density and hydraulic conductivity. As for the SHF configuration, the width of the mixing zone is mainly affected by uncertainty associated with the dispersion coefficient in the matrix. L_S is also majorly affected by the dispersion coefficient in the matrix, but the other uncertain parameters are also influencing it. All the uncertain parameters have distributed effects on M_S and Q_S^{total}.

Acknowledgment

Behzad Ataie-Ashtiani and Craig T. Simmons acknowledge support from the National Centre for Groundwater Research and Training, Australia. Behzad Ataie-Ashtiani also appreciates the support of the Research Office of the Sharif University of Technology, Iran. The authors are grateful for Behzad Mozafari from Sharif University of Technology for useful discussion on model development.

References

1. Arfib, B., Charlier, J.-B., 2016. Insights into saline intrusion and freshwater resources in coastal karstic aquifers using a lumped Rainfall–Discharge–Salinity model (the Port-Miou brackish spring, SE France). Journal of Hydrology 540, 148–161. https://doi.org/10.1016/j.jhydrol.2016.06.010
2. Ataie-Ashtiani, B., Werner, A.D., Simmons, C.T., Morgan, L.K., Lu, C., 2013. How important is the impact of land-surface inundation on seawater intrusion caused by sea-level rise? Hydrogeology Journal 21, 1673–1677. https://doi.org/10.1007/s10040-013-1021-0
3. Bakalowicz, M., El Hakim, M., El-Hajj, A., 2008. Karst groundwater resources in the countries of eastern Mediterranean: the example of Lebanon. Environmental Geology 54, 597–604. https://doi.org/10.1007/s00254-007-0854-z
4. Barragán, J.M., de Andrés, M., 2015. Analysis and trends of the world's coastal cities and agglomerations. Ocean & Coastal Management 114, 11–20. https://doi.org/10.1016/j.ocecoaman.2015.06.004
5. Blatman, G., Sudret, B., 2011. Adaptive sparse polynomial chaos expansion based on least angle regression. Journal of Computational Physics 230, 2345–2367. https://doi.org/10.1016/j.jcp.2010.12.021
6. Bear, J., Cheng, A.H.-D., Sorek, S., Ouazar, D., Herrera, I. (Eds.), 1999. Seawater Intrusion in Coastal Aquifers: Concepts, Methods and Practices, Theory and Applications of Transport in Porous Media. Springer Netherlands.
7. Beaujean, J., Nguyen, F., Kemna, A., Antonsson, A., Engesgaard, P., 2014. Calibration of seawater intrusion models: Inverse parameter estimation using surface electrical resistivity tomography and borehole data. Water Resources Research 50, 6828–6849. https://doi.org/10.1002/2013WR014020
8. Berre, I., Doster, F., Keilegavlen, E., 2018. Flow in Fractured Porous Media: A Review of Conceptual Models and Discretization Approaches. Transport in Porous Media. https://doi.org/10.1007/s11242-018-1171-6
9. Chen, Z., Auler, A.S., Bakalowicz, M., Drew, D., Griger, F., Hartmann, J., Jiang, G., Moosdorf, N., Richts, A., Stevanovic, Z., Veni, G., Goldscheider, N., 2017. The World Karst Aquifer Mapping project: concept, mapping procedure and map of Europe. Hydrogeology Journal 25, 771–785. https://doi.org/10.1007/s10040-016-1519-3
10. Ciriello, V., Federico, V.D., Riva, M., Cadini, F., Sanctis, J.D., Zio, E., Guadagnini, A., 2013. Polynomial chaos expansion for global sensitivity analysis applied to a model of radionuclide migration in a randomly heterogeneous aquifer. Stochastic Environmental Research and Risk Assessment 27, 945–954. https://doi.org/10.1007/s00477-012-0616-7
11. Comte, J.-C., Ofterdinger, U., Legchenko, A., Caulfield, J., Cassidy, R., González, J.A.M., 2018. Catchment-scale heterogeneity of flow and storage properties in a weathered/fractured hard rock aquifer from resistivity and magnetic resonance surveys: implications for groundwater flow paths and the distribution of residence times. Geological Society, London, Special Publications 479, SP479.11. https://doi.org/10.1144/SP479.11
12. Crestaux, T., Le Maıˆtre, O., Martinez, J.-M., 2009. Polynomial chaos expansion for sensitivity analysis. Reliability Engineering & System Safety 94, 1161–1172. https://doi.org/10.1016/j.ress.2008.10.008
13. Dai, H., Chen, X., Ye, M., Song, X., Zachara, J.M., 2017. A geostatistics-informed hierarchical sensitivity analysis method for complex groundwater flow and transport modeling. Water Resources Research 53, 4327–4343.

https://doi.org/10.1002/2016WR019756

14. De Rocquigny, E., 2012. Modelling Under Risk and Uncertainty: An Introduction to Statistical, Phenomenological and Computational Methods. John Wiley & Sons.
15. Dell'Oca, A., Riva, M., Guadagnini, A., 2017. Moment-based metrics for global sensitivity analysis of hydrological systems. Hydrology and Earth System Sciences 21, 6219–6234. https://doi.org/10.5194/hess-21-6219-2017
16. Deman, G., Konakli, K., Sudret, B., Kerrou, J., Perrochet, P., Benabderrahmane, H., 2016. Using sparse polynomial chaos expansions for the global sensitivity analysis of groundwater lifetime expectancy in a multi-layered hydrogeological model. Reliability Engineering & System Safety 147, 156–169. https://doi.org/10.1016/j.ress.2015.11.005
17. Deng, B., Wang, J., 2017. Saturated-unsaturated groundwater modeling using 3D Richards equation with a coordinate transform of nonorthogonal grids. Applied Mathematical Modelling 50, 39–52. https://doi.org/10.1016/j.apm.2017.05.021
18. Dietrich, P., Helmig, R., Sauter, M., Hötzl, H., Köngeter, J., Teutsch, G. (Eds.), 2005. Flow and Transport in Fractured Porous Media. Springer-Verlag, Berlin Heidelberg.
19. Dokou, Z., Karatzas, G.P., 2012. Saltwater intrusion estimation in a karstified coastal system using density-dependent modelling and comparison with the sharp-interface approach. Hydrological Sciences Journal 57, 985–999. https://doi.org/10.1080/02626667.2012.690070
20. Fahs, H., Hayek, M., Fahs, M., Younes, A., 2014. An efficient numerical model for hydrodynamic parameterization in 2D fractured dual-porosity media. Advances in Water Resources 63, 179–193. https://doi.org/10.1016/j.advwatres.2013.11.008
21. Fahs, M., Ataie-Ashtiani, B., Younes, A., Simmons, C.T., Ackerer, P., 2016. The Henry problem: New semianalytical solution for velocity-dependent dispersion. Water Resources Research 52, 7382–7407. https://doi.org/10.1002/2016WR019288
22. Fahs, M., Koohbor, B., Belfort, B., Ataie-Ashtiani, B., Simmons, C., Younes, A., Ackerer, P., 2018. A Generalized Semi-Analytical Solution for the Dispersive Henry Problem: Effect of Stratification and Anisotropy on Seawater Intrusion. Water 10, 230. https://doi.org/10.3390/w10020230
23. Fajraoui, N., Fahs, M., Younes, A., Sudret, B., 2017. Analyzing natural convection in porous enclosure with polynomial chaos expansions: Effect of thermal dispersion, anisotropic permeability and heterogeneity. International Journal of Heat and Mass Transfer 115, 205–224. https://doi.org/10.1016/j.ijheatmasstransfer.2017.07.003
24. Fajraoui, N., Mara, T.A., Younes, A., Bouhlila, R., 2012. Reactive Transport Parameter Estimation and Global Sensitivity Analysis Using Sparse Polynomial Chaos Expansion. Water, Air, & Soil Pollution 223, 4183–4197. https://doi.org/10.1007/s11270-012-1183-8
25. Fajraoui, N., Ramasomanana, F., Younes, A., Mara, T.A., Ackerer, P., Guadagnini, A., 2011. Use of global sensitivity analysis and polynomial chaos expansion for interpretation of nonreactive transport experiments in laboratory-scale porous media. Water Resources Research 47. https://doi.org/10.1029/2010WR009639
26. Fidelibus, M.D., Calò, G., Tinelli, R., Tulipano, L., 2011. Salt ground waters in the Salento karstic coastal aquifer (Apulia, Southern Italy), in: Advances in the Research of Aquatic Environment, Environmental Earth Sciences. Springer, Berlin, Heidelberg, pp. 407–415. https://doi.org/10.1007/978-3-642-19902-8_48
27. Fischer, P., Jardani, A., Cardiff, M., Lecoq, N., Jourde, H., 2018. Hydraulic analysis of harmonic pumping tests in frequency and time domains for identifying the conduits networks in a karstic aquifer. Journal of Hydrology 559, 1039–1053. https://doi.org/10.1016/j.jhydrol.2018.03.010

28. Grillo, A., Logashenko, D., Stichel, S., Wittum, G., 2010. Simulation of density-driven flow in fractured porous media. Advances in Water Resources 33, 1494–1507. https://doi.org/10.1016/j.advwatres.2010.08.004
29. Guevara Morel, C.R., van Reeuwijk, M., Graf, T., 2015. Systematic investigation of non-Boussinesq effects in variable-density groundwater flow simulations. Journal of Contaminant Hydrology 183, 82–98. https://doi.org/10.1016/j.jconhyd.2015.10.004
30. Herckenrath, D., Langevin, C.D., Doherty, J., 2011. Predictive uncertainty analysis of a saltwater intrusion model using null-space Monte Carlo. Water Resources Research 47. https://doi.org/10.1029/2010WR009342
31. Hirthe, E.M., Graf, T., 2015. Fracture network optimization for simulating 2D variable-density flow and transport. Advances in Water Resources 83, 364–375. https://doi.org/10.1016/j.advwatres.2015.07.001
32. Homma, T., Saltelli, A., 1996. Importance measures in global sensitivity analysis of nonlinear models. Reliability Engineering & System Safety 52, 1–17. https://doi.org/10.1016/0951-8320(96)00002-6
33. Hu, C., Youn, B.D., 2011. Adaptive-sparse polynomial chaos expansion for reliability and design of complex engineering systems. Structural and Multidisciplinary Optimization 43, 419–442. https://doi.org/10.1007/s00158-010-0568-9
34. IOC/UNESCO, IMO, FAO, UNDP., 2011. A Blueprint for Ocean and Coastal Sustainability, IOC/UNESCO. Paris.
35. Iooss, B., Lemaître, P., 2015. A Review on Global Sensitivity Analysis Methods, in: Dellino, G., Meloni, C. (Eds.), Uncertainty Management in Simulation-Optimization of Complex Systems. Springer US, Boston, MA, pp. 101–122. https://doi.org/10.1007/978-1-4899-7547-8_5
36. Jerbi, C., Fourno, A., Noetinger, B., Delay, F., 2017. A new estimation of equivalent matrix block sizes in fractured media with two-phase flow applications in dual porosity models. Journal of Hydrology 548, 508–523. https://doi.org/10.1016/j.jhydrol.2017.03.028
37. Jia, W., McPherson, B.J., Pan, F., Xiao, T., Bromhal, G., 2016. Probabilistic analysis of CO2 storage mechanisms in a CO2-EOR field using polynomial chaos expansion. International Journal of Greenhouse Gas Control 51, 218–229. https://doi.org/10.1016/j.ijggc.2016.05.024
38. Kerrou, J., Renard, P., 2010. A numerical analysis of dimensionality and heterogeneity effects on advective dispersive seawater intrusion processes. Hydrogeology Journal 18, 55–72. https://doi.org/10.1007/s10040-009-0533-0
39. Ketabchi, H., Mahmoodzadeh, D., Ataie-Ashtiani, B., Simmons, C.T., 2016. Sea-level rise impacts on seawater intrusion in coastal aquifers: Review and integration. Journal of Hydrology 535, 235–255. https://doi.org/10.1016/j.jhydrol.2016.01.083
40. Konakli, K., Sudret, B., 2016. Global sensitivity analysis using low-rank tensor approximations. Reliability Engineering & System Safety 156, 64–83. https://doi.org/10.1016/j.ress.2016.07.012
41. Le Gratiet, L., Marelli, S., Sudret, B., 2017. Metamodel-Based Sensitivity Analysis: Polynomial Chaos Expansions and Gaussian Processes, in: Ghanem, R., Higdon, D., Owhadi, H. (Eds.), Handbook of Uncertainty Quantification. Springer International Publishing, Cham, pp. 1289–1325. https://doi.org/10.1007/978-3-319-12385-1_38
42. Llopis-Albert, C., Merigó, J.M., Xu, Y., 2016. A coupled stochastic inverse/sharp interface seawater intrusion approach for coastal aquifers under groundwater parameter uncertainty. Journal of Hydrology 540, 774–783. https://doi.org/10.1016/j.jhydrol.2016.06.065
43. Lu, C., Chen, Y., Zhang, C., Luo, J., 2013. Steady-state freshwater–seawater mixing

zone in stratified coastal aquifers. Journal of Hydrology 505, 24–34. https://doi.org/10.1016/j.jhydrol.2013.09.017

44. MacAllister, D., Jackson, M.D., Butler, A.P., Vinogradov, J., 2018. Remote Detection of Saline Intrusion in a Coastal Aquifer Using Borehole Measurements of Self-Potential. Water Resources Research 54, 1669–1687. https://doi.org/10.1002/2017WR021034
45. Maina, F.Z., Guadagnini, A., 2018. Uncertainty Quantification and Global Sensitivity Analysis of Subsurface Flow Parameters to Gravimetric Variations During Pumping Tests in Unconfined Aquifers. Water Resources Research 54, 501–518. https://doi.org/10.1002/2017WR021655
46. Marelli, S., Sudret, B., 2014. UQLab: A Framework for Uncertainty Quantification in Matlab. American Society of Civil Engineers, pp. 2554–2563. https://doi.org/10.1061/9780784413609.257
47. Mehdizadeh, S.S., Werner, A.D., Vafaie, F., Badaruddin, S., 2014. Vertical leakage in sharp-interface seawater intrusion models of layered coastal aquifers. Journal of Hydrology 519, 1097–1107. https://doi.org/10.1016/j.jhydrol.2014.08.027
48. Meng, J., Li, H., 2017. Efficient Uncertainty Quantification for Unconfined Flow in Heterogeneous Media with the Sparse Polynomial Chaos Expansion. Transport in Porous Media. https://doi.org/10.1007/s11242-017-0974-1
49. Miller, K.L., Berg, S.J., Davison, J.H., Sudicky, E.A., Forsyth, P.A., 2018. Efficient uncertainty quantification in fully-integrated surface and subsurface hydrologic simulations. Advances in Water Resources 111, 381–394. https://doi.org/10.1016/j.advwatres.2017.10.023
50. Mozafari, B., Fahs, M., Ataie-Ashtiani, B., Simmons, C.T., Younes, R., 2018. On the use of COMSOL Multiphysics for seawater intrusion in fractured coastal aquifers. E3S Web of Conferences 54, 00020. https://doi.org/10.1051/e3sconf/20185400020
51. Perriquet, M., Leonardi, V., Henry, T., Jourde, H., 2014. Saltwater wedge variation in a non-anthropogenic coastal karst aquifer influenced by a strong tidal range (Burren, Ireland). Journal of Hydrology 519, 2350–2365. https://doi.org/10.1016/j.jhydrol.2014.10.006
52. Pool, M., Post, V.E.A., Simmons, C.T., 2015. Effects of tidal fluctuations and spatial heterogeneity on mixing and spreading in spatially heterogeneous coastal aquifers. Water Resources Research 51, 1570–1585. https://doi.org/10.1002/2014WR016068
53. Rajabi, M.M., Ataie-Ashtiani, B., 2014. Sampling efficiency in Monte Carlo based uncertainty propagation strategies: Application in seawater intrusion simulations. Advances in Water Resources 67, 46–64. https://doi.org/10.1016/j.advwatres.2014.02.004
54. Rajabi, M.M., Ataie-Ashtiani, B., Simmons, C.T., 2015. Polynomial chaos expansions for uncertainty propagation and moment independent sensitivity analysis of seawater intrusion simulations. Journal of Hydrology 520, 101–122. https://doi.org/10.1016/j.jhydrol.2014.11.020
55. Ramasomanana, F., Fahs, M., Baalousha, H.M., Barth, N., Ahzi, S., 2018. An Efficient ELLAM Implementation for Modeling Solute Transport in Fractured Porous Media. Water, Air, & Soil Pollution 229, 46. https://doi.org/10.1007/s11270-018-3690-8
56. Ren, F., Ma, G., Wang, Y., Li, T., Zhu, H., 2017. Unified pipe network method for simulation of water flow in fractured porous rock. Journal of Hydrology 547, 80–96. https://doi.org/10.1016/j.jhydrol.2017.01.044
57. Riva, M., Guadagnini, A., Dell'Oca, A., 2015. Probabilistic assessment of seawater intrusion under multiple sources of uncertainty. Advances in Water Resources 75, 93–

104. https://doi.org/10.1016/j.advwatres.2014.11.002
58. Saltelli, A., 2002. Making best use of model evaluations to compute sensitivity indices. Computer Physics Communications 145, 280–297. https://doi.org/10.1016/S0010-4655(02)00280-1
59. Sarkar, S., Witteveen, J.A., 2016. Uncertainty Quantification In Computational Science: Theory And Application In Fluids And Structural Mechanics. World Scientific.
60. Sayler, C., Cardiff, M., Fort, M.D., 2018. Understanding the Geometry of Connected Fracture Flow with Multiperiod Oscillatory Hydraulic Tests. Groundwater 56, 276–287. https://doi.org/10.1111/gwat.12580
61. Sebben, M.L., Werner, A.D., Graf, T., 2015. Seawater intrusion in fractured coastal aquifers: A preliminary numerical investigation using a fractured Henry problem. Advances in Water Resources 85, 93–108. https://doi.org/10.1016/j.advwatres.2015.09.013
62. Shao, Q., Younes, A., Fahs, M., Mara, T.A., 2017. Bayesian sparse polynomial chaos expansion for global sensitivity analysis. Computer Methods in Applied Mechanics and Engineering 318, 474–496. https://doi.org/10.1016/j.cma.2017.01.033
63. Shi, W., Lu, C., Ye, Y., Wu, J., Li, L., Luo, J., 2018. Assessment of the impact of sea-level rise on steady-state seawater intrusion in a layered coastal aquifer. Journal of Hydrology 563, 851–862. https://doi.org/10.1016/j.jhydrol.2018.06.046
64. Simmons, C.T., Fenstemaker, T.R., Sharp, J.M., 2001. Variable-density groundwater flow and solute transport in heterogeneous porous media: approaches, resolutions and future challenges. Journal of Contaminant Hydrology 52, 245–275. https://doi.org/10.1016/S0169-7722(01)00160-7
65. Sobol′, I.M., 2001. Global sensitivity indices for nonlinear mathematical models and their Monte Carlo estimates. Mathematics and Computers in Simulation, The Second IMACS Seminar on Monte Carlo Methods 55, 271–280. https://doi.org/10.1016/S0378-4754(00)00270-6
66. Stoeckl, L., Houben, G.J., Dose, E.J., 2015. Experiments and modeling of flow processes in freshwater lenses in layered island aquifers: Analysis of age stratification, travel times and interface propagation. Journal of Hydrology 529, 159–168. https://doi.org/10.1016/j.jhydrol.2015.07.019
67. Sudret, B., 2008. Global sensitivity analysis using polynomial chaos expansions. Reliability Engineering & System Safety 93, 964–979. https://doi.org/10.1016/j.ress.2007.04.002
68. Szymkiewicz, A., Gumuła-Kawęcka, A., Šimůnek, J., Leterme, B., Beegum, S., Jaworska-Szulc, B., Pruszkowska-Caceres, M., Gorczewska-Langner, W., Angulo-Jaramillo, R., Jacques, D., 2018. Simulations of freshwater lens recharge and salt/freshwater interfaces using the HYDRUS and SWI2 packages for MODFLOW. Journal of Hydrology and Hydromechanics 66, 246–256. https://doi.org/10.2478/johh-2018-0005
69. Werner, A.D., Bakker, M., Post, V.E.A., Vandenbohede, A., Lu, C., Ataie-Ashtiani, B., Simmons, C.T., Barry, D.A., 2013. Seawater intrusion processes, investigation and management: Recent advances and future challenges. Advances in Water Resources 51, 3–26. https://doi.org/10.1016/j.advwatres.2012.03.004
70. Xu, Z., Hu, B.X., Ye, M., 2018. Numerical modeling and sensitivity analysis of seawater intrusion in a dual-permeability coastal karst aquifer with conduit networks. Hydrology and Earth System Sciences 22, 221–239. https://doi.org/10.5194/hess-22-221-2018
71. Younes, A., Delay, F., Fajraoui, N., Fahs, M., Mara, T.A., 2016. Global sensitivity

analysis and Bayesian parameter inference for solute transport in porous media colonized by biofilms. Journal of Contaminant Hydrology 191, 1–18. https://doi.org/10.1016/j.jconhyd.2016.04.007

72. Younes, A., Mara, T.A., Fajraoui, N., Lehmann, F., Belfort, B., Beydoun, H., 2013. Use of Global Sensitivity Analysis to Help Assess Unsaturated Soil Hydraulic Parameters. Vadose Zone Journal 12, 0. https://doi.org/10.2136/vzj2011.0150
73. Younes, A., Zaouali, J., Lehmann, F., Fahs, M., 2018. Sensitivity and identifiability of hydraulic and geophysical parameters from streaming potential signals in unsaturated porous media. Hydrology and Earth System Sciences 22, 3561–3574. https://doi.org/10.5194/hess-22-3561-2018
74. Younes, A., Fahs, M., Ahmed, S., 2009. Solving density driven flow problems with efficient spatial discretizations and higher-order time integration methods. Advances in Water Resources 32, 340–352. https://doi.org/10.1016/j.advwatres.2008.11.003

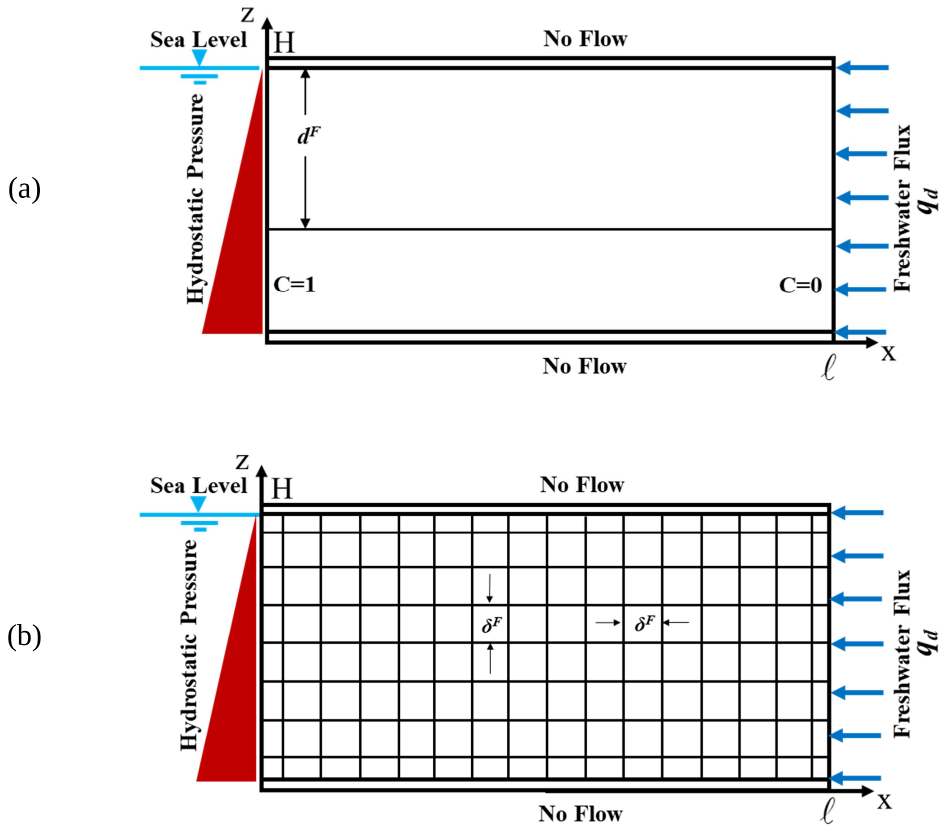

Fig. 1. Conceptual model of the fractured Henry Problem: (a) Single horizontal fracture configuration (SHF) and (b) Network of orthogonal fractures configuration (NOF).

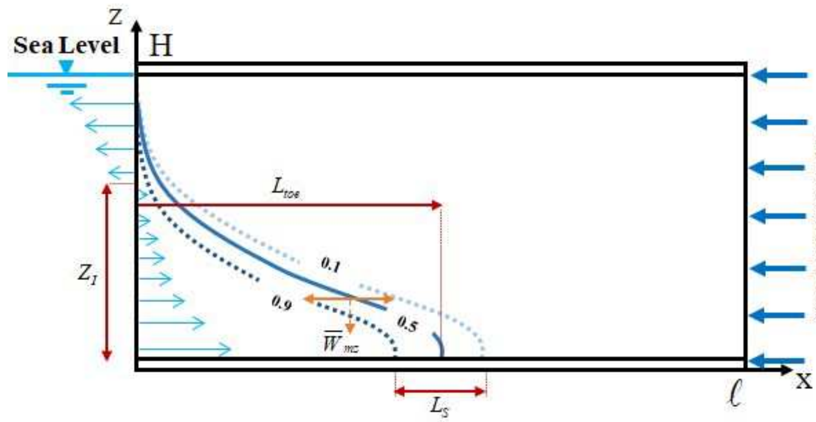

Fig. 2. Schematic representation of the SWI metrics.

(a)

(b)

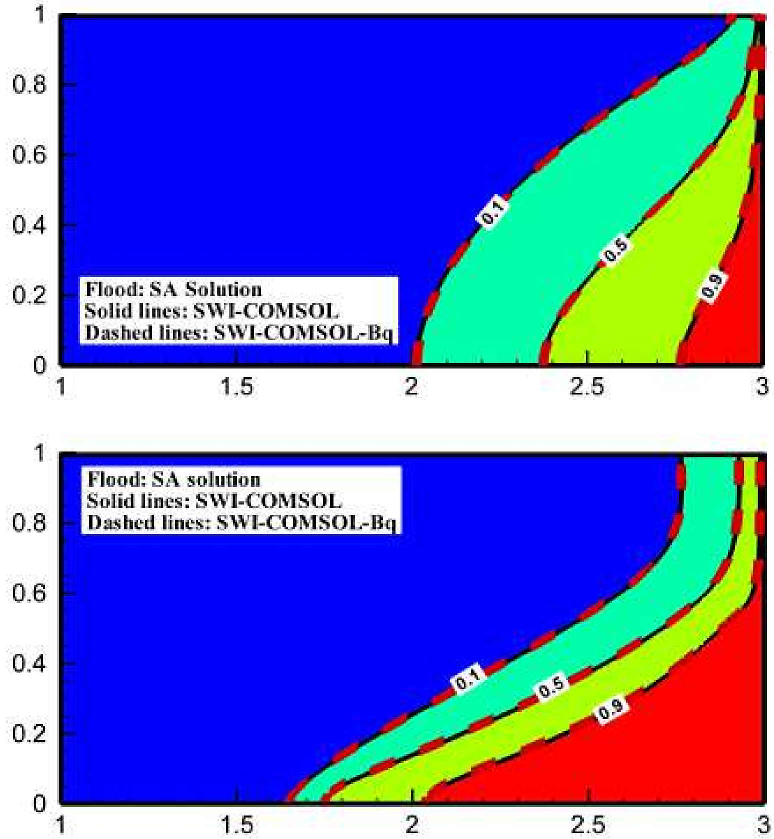

Fig. 3. Isochlors obtained using the semi-analytical solution (SA) and COMSOL model (with and without Boussinesq approximation) for the homogenous test cases: (a) diffusive case and (b) dispersive case.

(a)

(b)

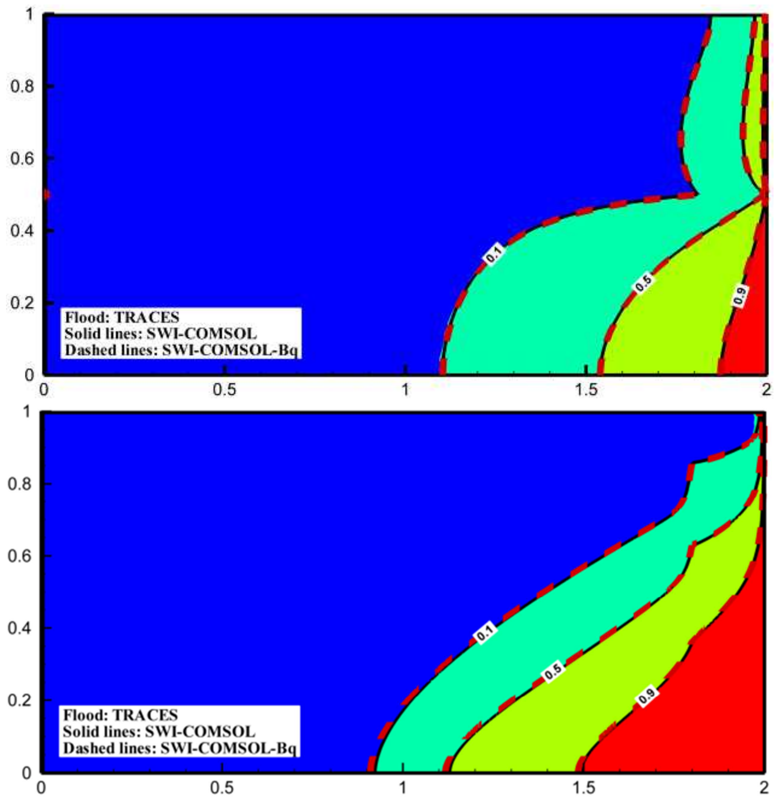

Fig. 4. Isochlors obtained using TRACES (in-house code) and COMSOL model (with and without Boussinesq approximation) for the fractured test cases: a) single horizontal fracture and b) single vertical fracture.

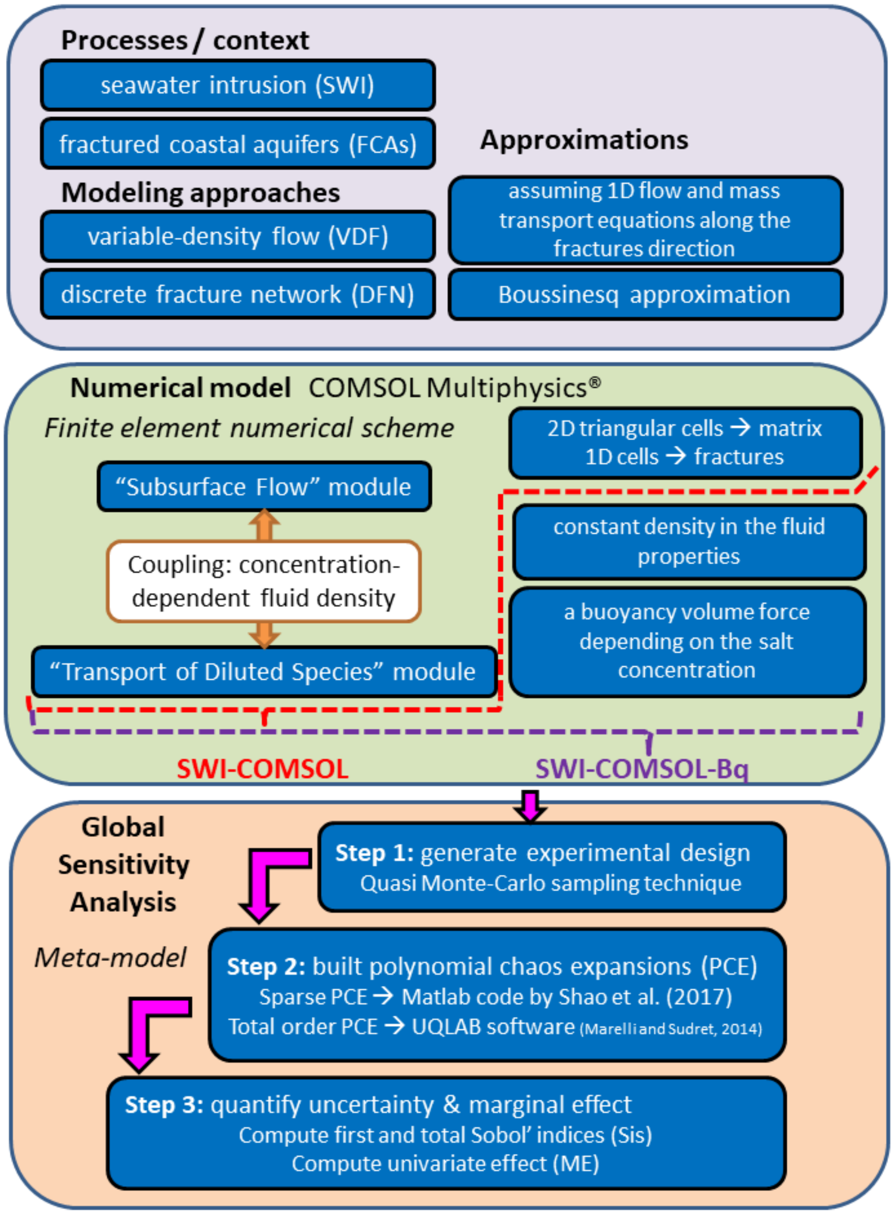

Fig. 5. A flowchart describing the methodology and approaches used to perform the global sensitivity analysis: The first block (in purple) describes the physical processes and the corresponding mathematical models used in this study; The second block (in olive-green) presents the finite element model used to simulate the physical processes (COMSOL with and without Boussinesq approximation); The third block (in orange) describes the approach used to perform global sensitivity analysis (polynomial chaos expansion as meta-model and Sobol's indices as sensitivity metrics).

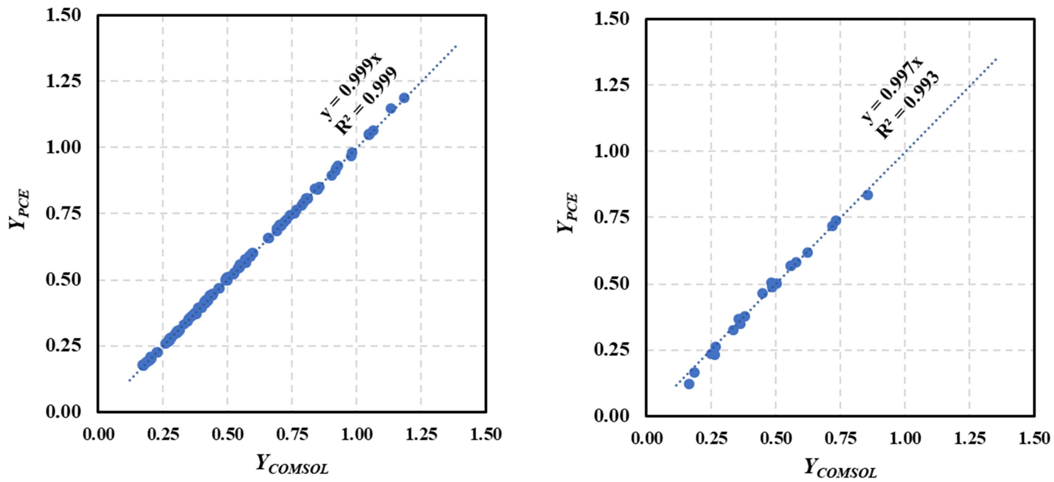

a) The length of the saltwater toe (L_{toe}).

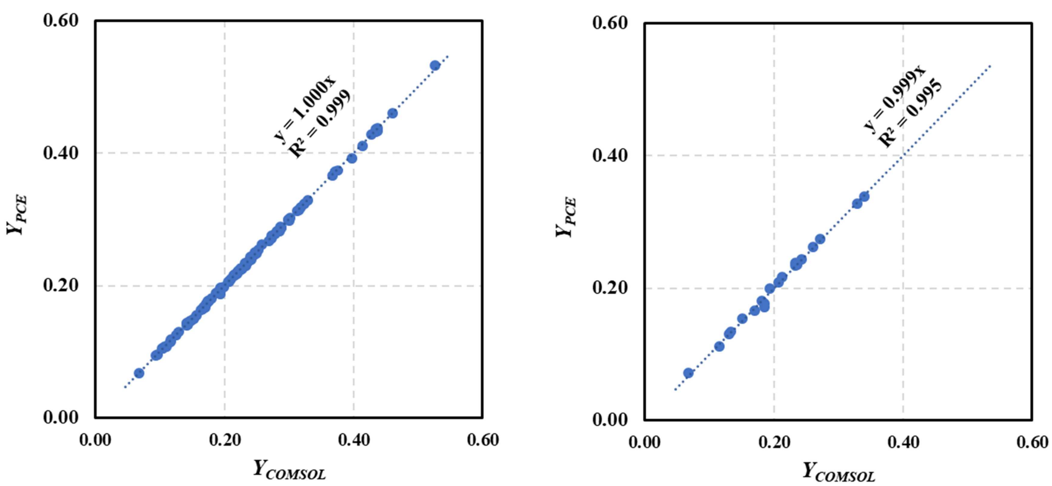

b) The dimensionless mass of salt persisting in the aquifer $\left(M_S\right)$.

Fig. 6. Comparison between the PCE surrogate model and physical (COMSOL) model for the SHF configuration: On the left side, 100 samples used for the experimental design and on the right side, 20 simulations which do not coincide with the experimental design (R^2 is the coefficient of determination).

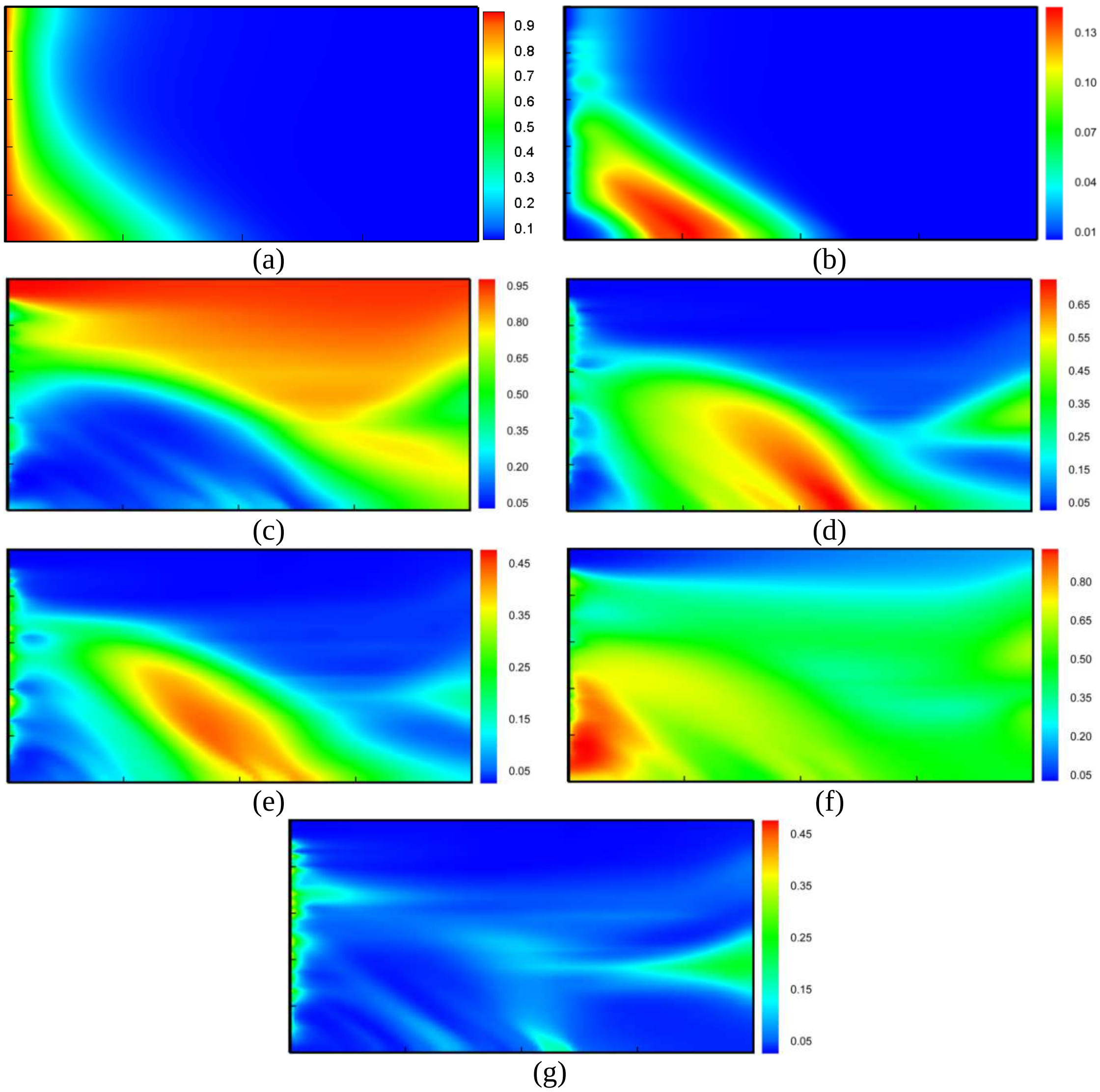

Fig. 7. GSA results for the spatial distribution of the salt concentration (SHF configuration): (a) mean salt concentration (b) variance of the salt concentration, (c) total SI of α_L^M, (d) total SI of K^F, (e) total SI of e^F, (f) total SI index of d^F and (g) total SI index of α_L^F.

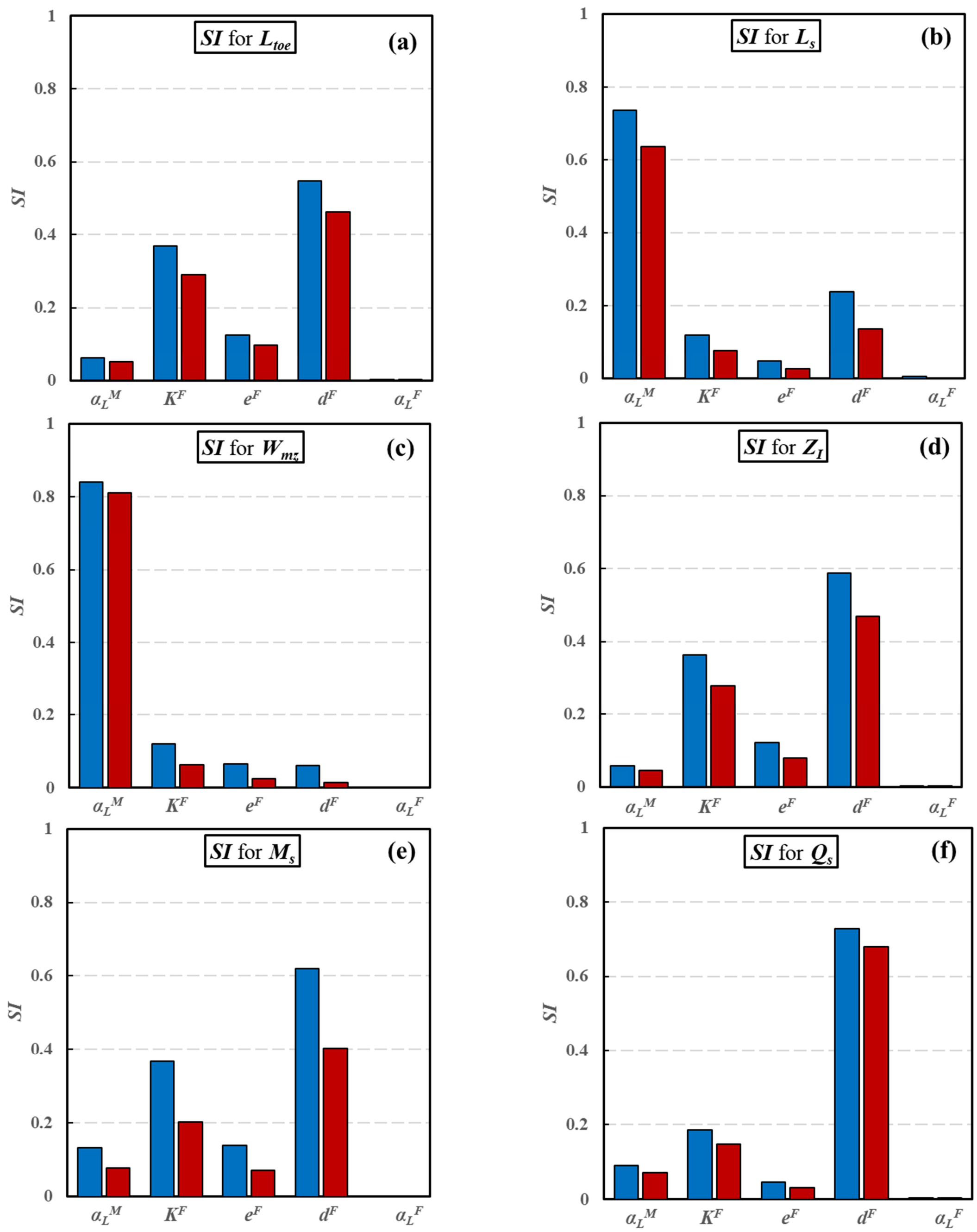

Fig. 8. Total (blue) and first order (red) SIs for the SHF configuration: (a) L_{toe}, (b) L_S, (c) $\overline{W}_{mz}$, (d) Z_I, (e) M_S and (f) Q_S^{total}.

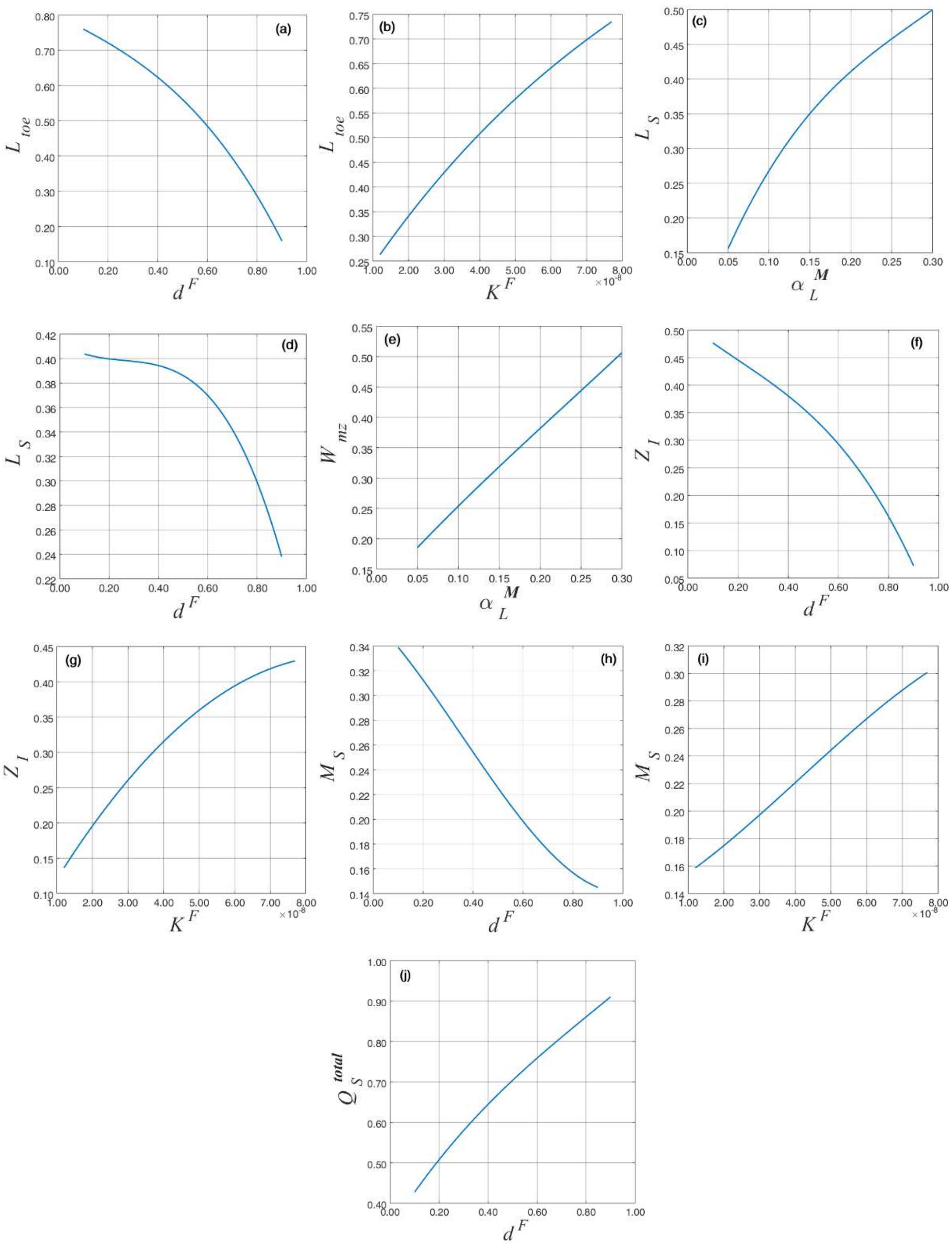

Fig. 9. The marginal effects of uncertain parameters on SWI metrics for the SHF configuration.

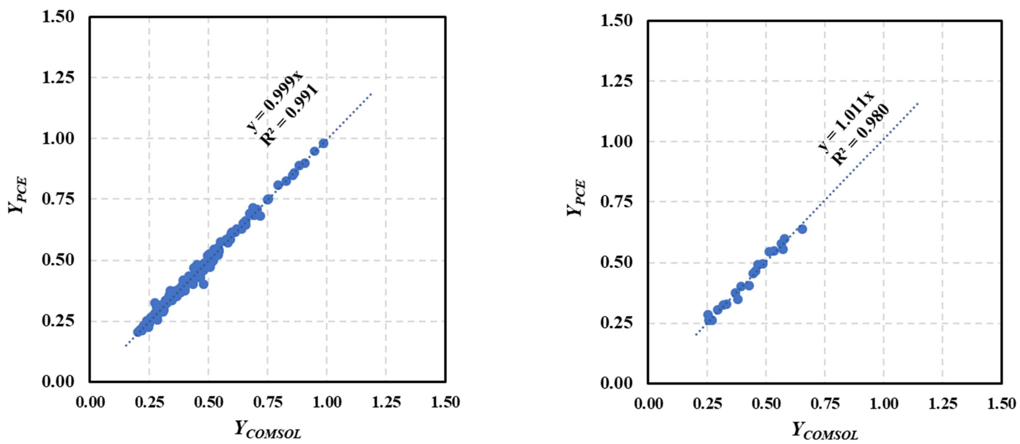

a) The length of the saltwater toe (L_{toe})

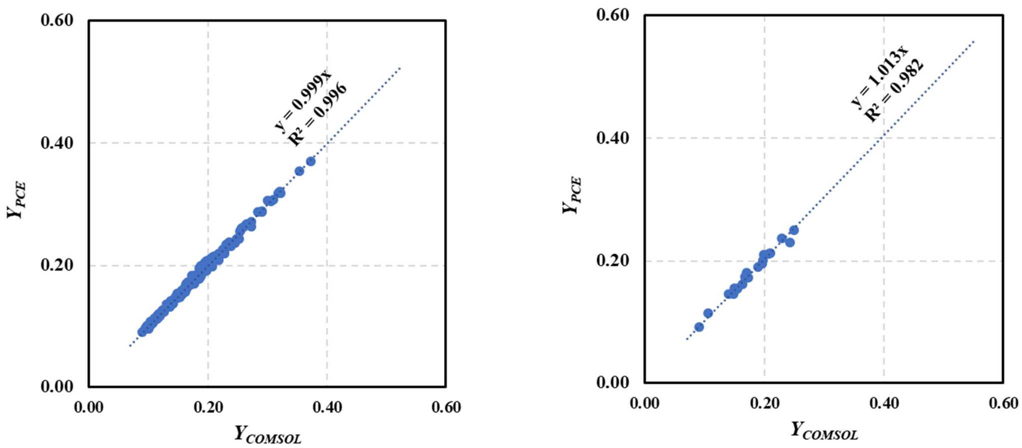

b) The dimensionless mass of salt persisting in the aquifer (M_S).

Fig. 10. Comparison between the PCE surrogate and physical (COMSOL) models for the NOF configuration: On the left side, 200 samples used for the experimental design and on the right side, 20 simulations which do not coincide with the experimental design.

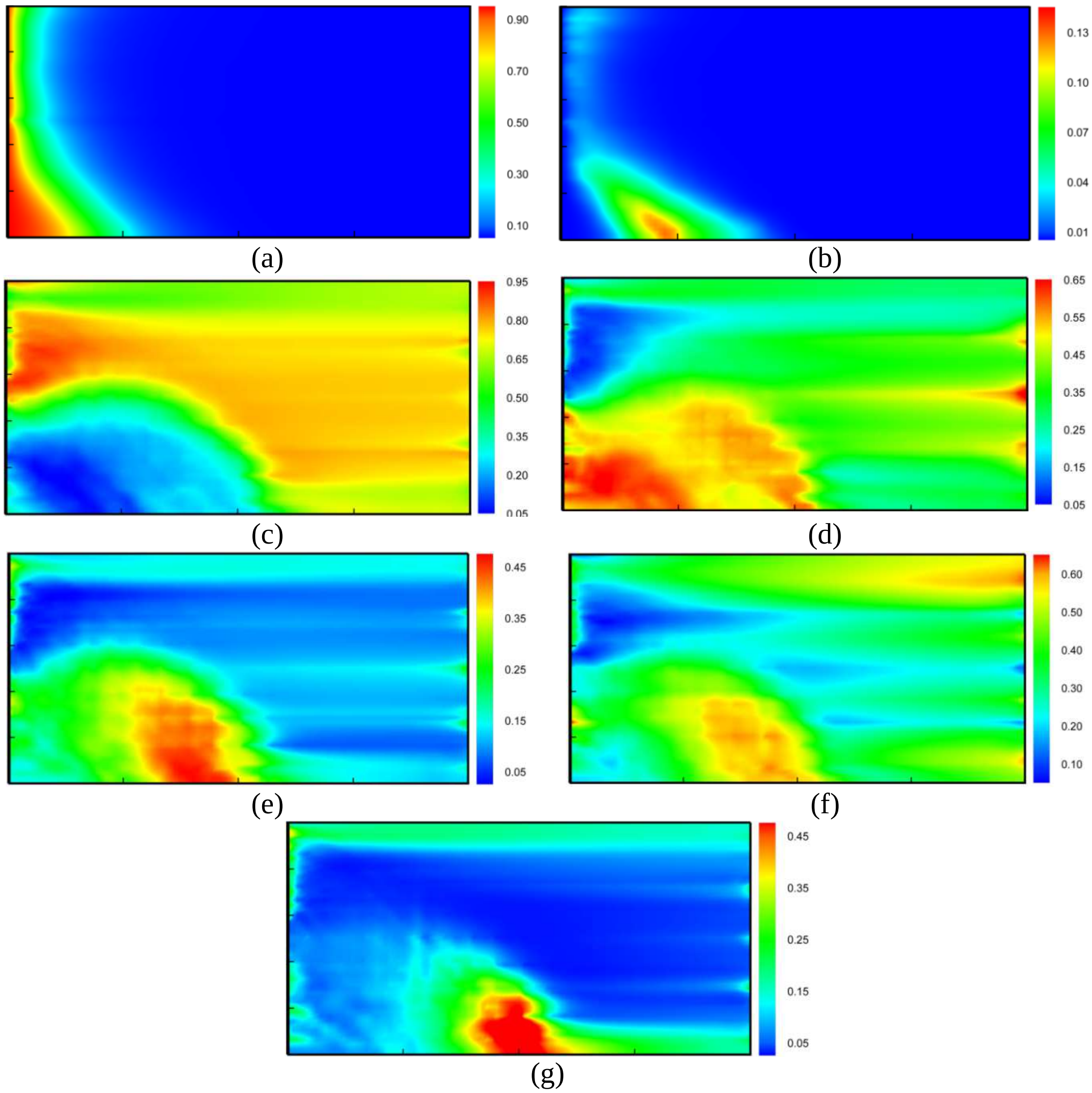

Fig. 11. GSA results for the spatial distribution of the salt concentration (NOF configuration): (a) mean salt concentration (b) variance of the salt concentration, (c) total SI of α_L^M, (d) total SI of K^F, (e) total SI of e^F, (f) total SI index of δ^F and (g) total SI index of α_L^F

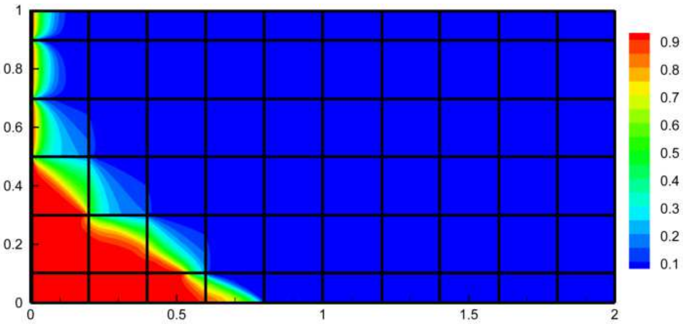

Fig. 12. Isochlors distribution for the NOF configuration ($\alpha_L^M = \alpha_L^F = 0.05m$; $K^F = 0.07m/s$; $e^F = 0.1mm$; $\delta^F = 0.2m$, others parameters are the same as Table 3).

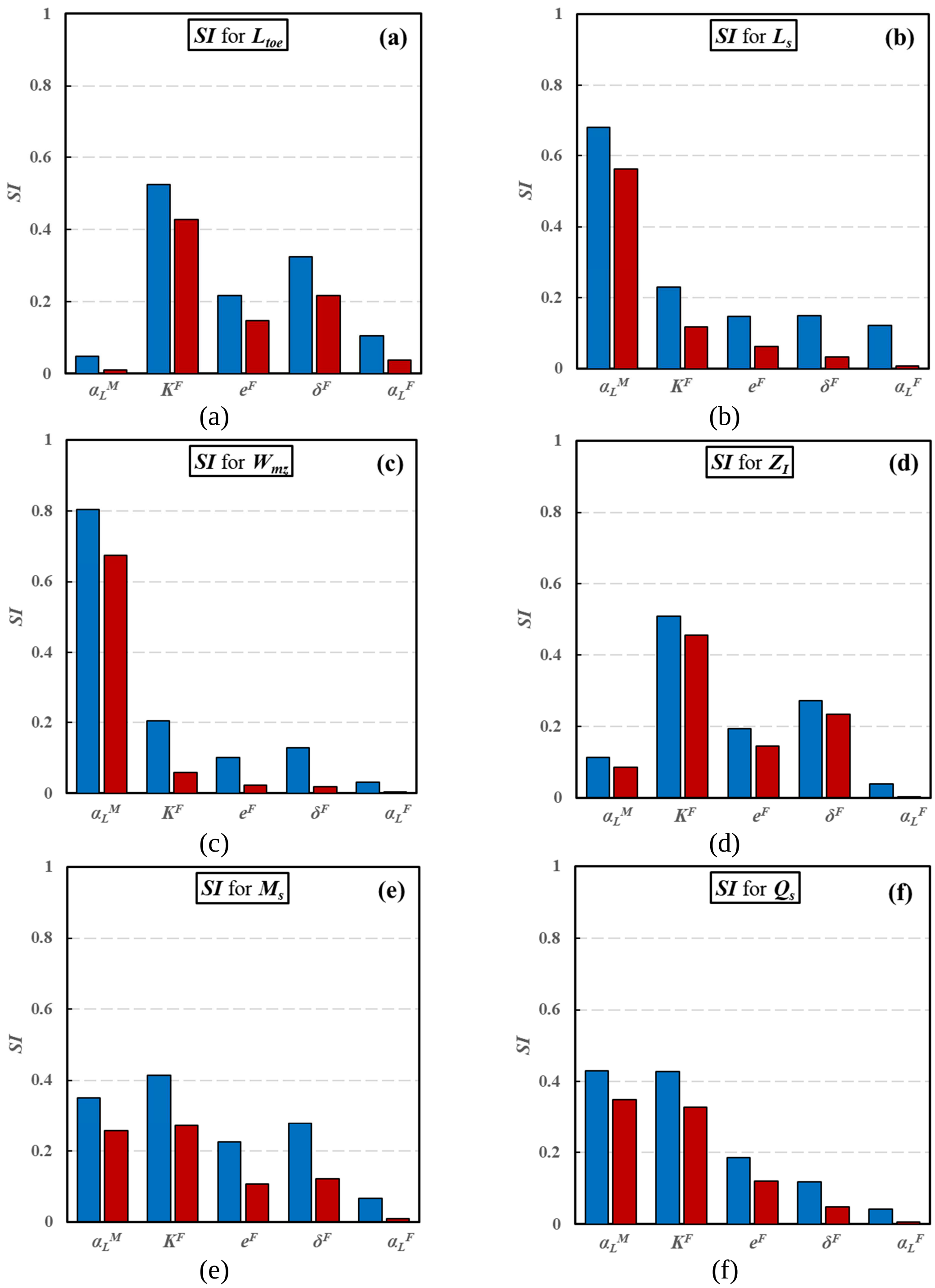

Fig. 13. Total (blue) and first order (red) SIs for the NOF configuration: (a) L_{toe}, (b) L_S, (c) $\overline{W}_{mz}$, (d) Z_I, (e) M_S and (f) Q_S^{total}.

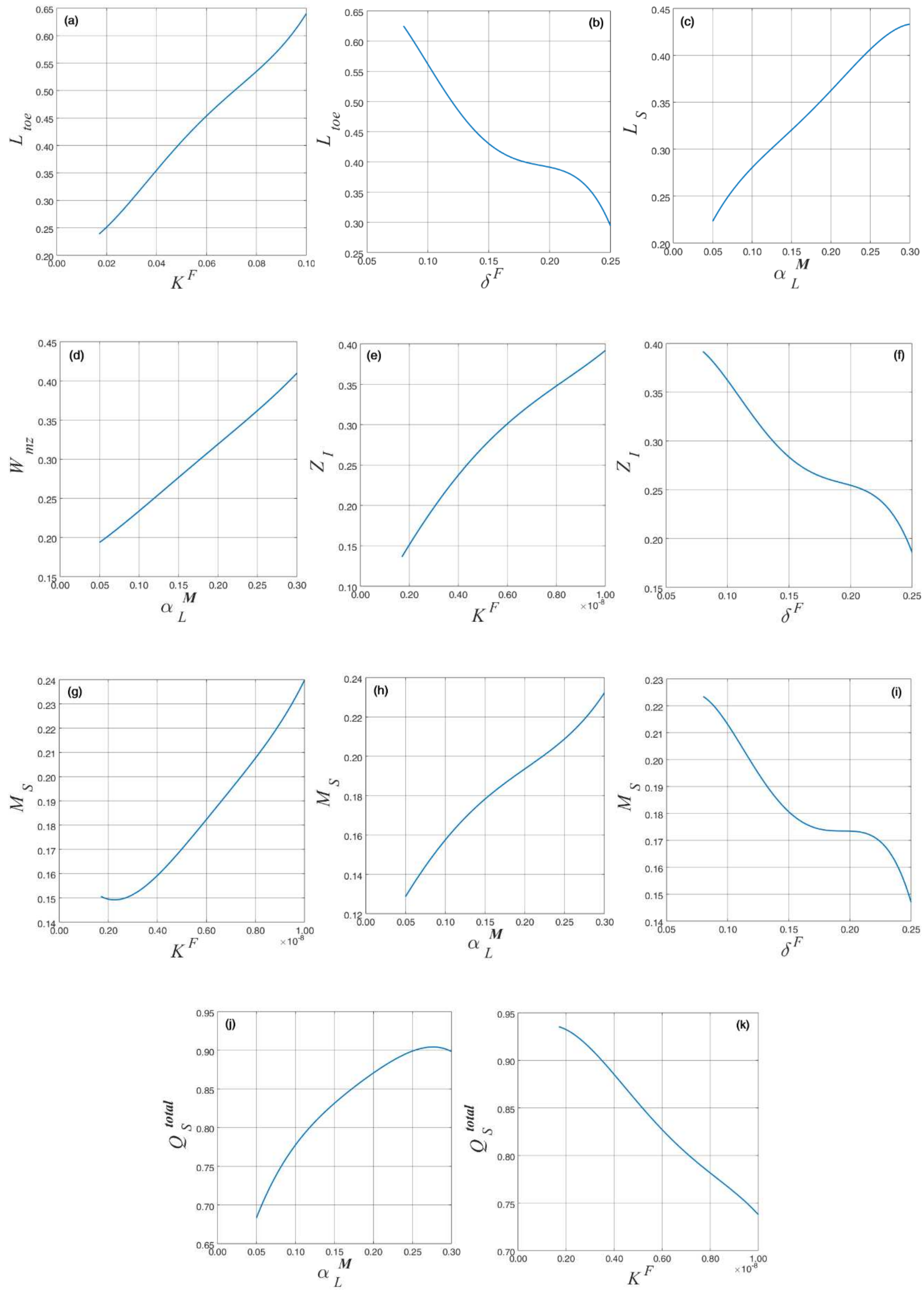

Fig. 14. The marginal effects of uncertain parameters on SWI metrics for the NOF configuration.

Table 1. Physical parameters used for the validation of homogeneous and fractured cases

Parameters	Homogenous cases		Fractured cases
ρ_1 *[kg/m³]*	1,025		1,025
ρ_0 *[kg/m³]*	1,000		1,000
q_d *[m²/s]*	6.6×10^{-5}		6.6×10^{-6}
H *[m]*	1		1
ℓ *[m]*	3		2
K^M *[m/s]*	1.001×10^{-2}		2.5×10^{-4} Horizontal Fracture 1.0×10^{-3} Vertical Fracture
K^F *[m/s]*	-		7.72×10^{-1}
ε^M *[-]*	0.35		0.2
ε^F *[-]*	-		1.0
e^F *[m]*	-		0.001
d^F *[m]*	-		0.5
D_m *[m²/s]*	18.86×10^{-6} 9.43×10^{-8}	Diffusive case Dispersive case	18.86×10^{-7} Horizontal Fracture 1.0×10^{-6} Vertical Fracture
α_L^M *[m]*	0	Diffusive case	0
	0.1	Dispersive case	
α_T^M *[m]*	0	Diffusive case	0
	0.01	Dispersive case	
α_L^F *[m]*	-		0
α_T^F *[m]*	-		0

Table 2. SWI metrics for the validation cases: Semi-analytical solution (S-Anl), SWI-COMSOL (Co-st) and SWI-COMSOL-Bq (CO-Bq). The width of the mixing zone for the homogenous case is calculated vertically as in *Fahs et al. [2016]*.

Metrics	Homogenous Diffusive			Homogenous Dispersive			Fractured (Horizontal)		
	S-Anl	CO-St	CO-Bq	S-Anl	CO-St	CO-Bq	TRACES	CO-St	CO-Bq
L_{toe}	0.624	0.626	0.625	1.256	1.253	1.251	0.460	0.461	0.460
L_S	0.751	0.754	0.752	0.368	0.392	0.391	0.768	0.777	0.776
$\overline{W}_{mz}$	0.757	0.763	0.760	0.295	0.295	0.294	0.451	0.455	0.455
Z_I	0.419	0.430	0.429	0.527	0.521	0.519	0.492	0.478	0.478
M_S	0.109	0.109	0.109	0.150	0.151	0.150	0.113	0.114	0.114
Q_S^{total}	1.068	0.970	0.976	1.061	1.037	1.049	0.625	0.618	0.622

Table 3. Values and ranges of variability of the parameters used for the GSA.

Parameters	Configuration SHF	Configuration NOF
ρ_1 *[kg/m³]*	1,025	1,025
ρ_0 *[kg/m³]*	1,000	1,000
q_d *[m²/s]*	6.6×10^{-6}	6.6×10^{-6}
H *[m]*	1	1
ℓ *[m]*	2	2
K^M *[m/s]*	2.49×10^{-5}	2.49×10^{-5}
K^F *[m/s]*	$[1.17\times10^{-1} - 7.65\times10^{-1}]$	$[1.86\times10^{-2} - 1.17\times10^{-1}]$
ε^M *[-]*	0.2	0.2
ε^F *[-]*	1.0	1.0
e^F *[m]*	$[3.8\times10^{-4} - 9.7\times10^{-4}]$	$[3.8\times10^{-4} - 9.7\times10^{-4}]$
d^F *[m]*	$[0.1 - 0.9]$	-
δ^F *[m]*	-	$[0.08 - 0.25]$
D_m *[m²/s]*	10^{-9}	10^{-9}
α_L^M *[m]*	$[0.05 - 0.3]$	$[0.05 - 0.3]$
α_T^M *[m]*	$0.1\times\alpha_L^M$	$0.1\times\alpha_L^M$
α_L^F *[m]*	$[0.05 - 0.3]$	$[0.05 - 0.3]$
α_T^F *[m]*	0	0

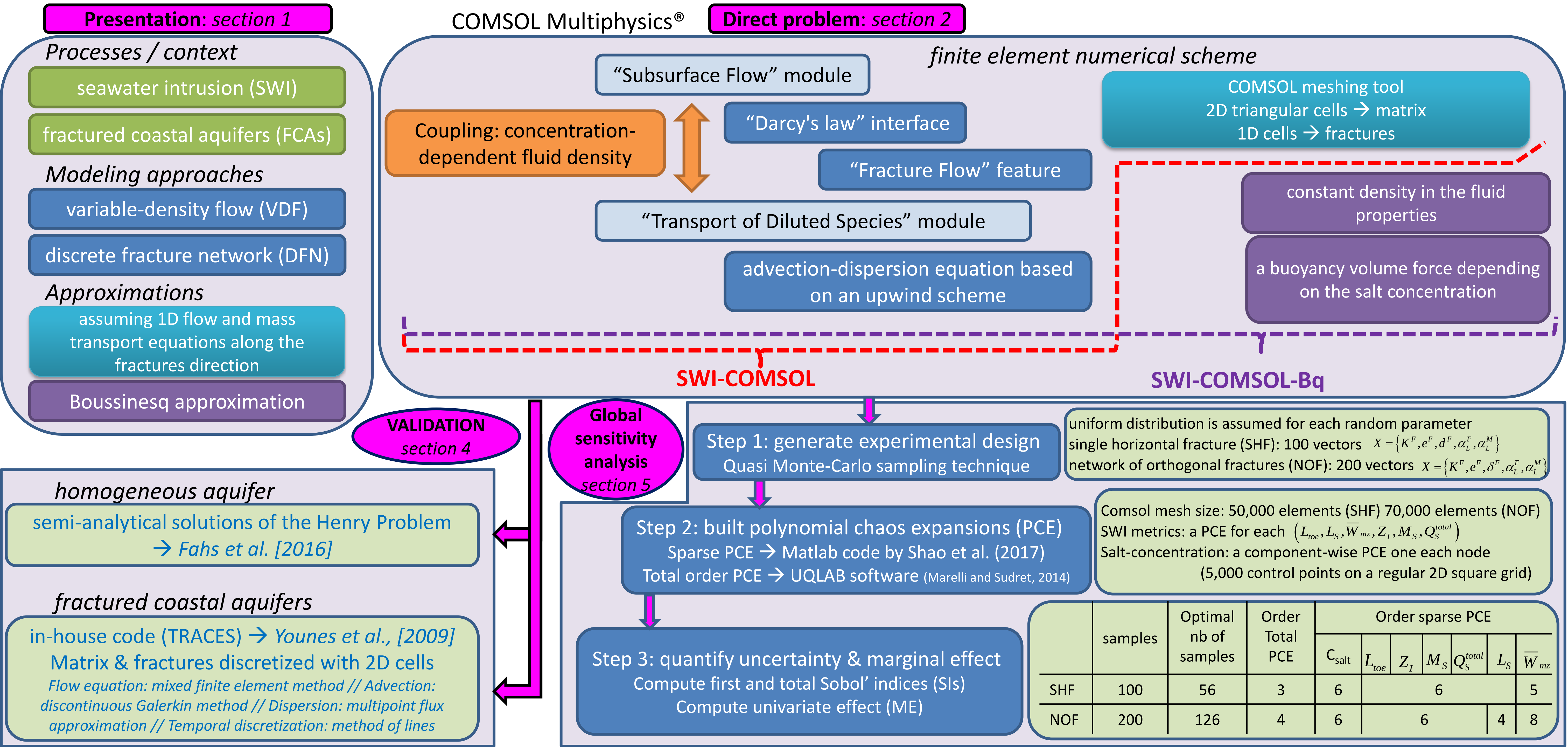

	samples	Optimal nb of samples	Order Total PCE	Order sparse PCE						
				C_{salt}	L_{toe}	Z_I	M_S	Q_S^{total}	L_S	$\overline{W}_{mz}$
SHF	100	56	3	6	6					5
NOF	200	126	4	6	6				4	8